CHAPTER 5

Electrical Capacitance, Electrical Resistance, and Positron Emission Tomography Techniques and Their Applications in Multi-Phase Flow Systems

Fei Wang[1], **Qussai Marashdeh**[1], **Liang-Shih Fan**[1,*] and **Richard A Williams**[2,*]

Contents

1 Department of Chemical and Biomolecular Engineering, The Ohio State University, Columbus, OH 43210, USA

2 Institute of Particle Science and Engineering, School of Process, Environmental and Materials Engineering, University of Leeds LS2 9JT, UK

*Corresponding author
E-mail address: fan@chbmeng.ohio-state.edu
E-mail address: r.a.williams@leeds.ac.uk

Advances in Chemical Engineering, Volume 37
ISSN: 0065-2377, DOI 10.1016/S0065-2377(09)03705-3

Abstract This article describes the recent progress in research and development on electrical capacitance tomography (ECT), electrical resistance tomography (ERT), and positron emission tomography (PET). Specifically, the article highlights several aspects of the three technologies and illustrates their application and performance through selected demonstration cases studies. The principles and results from the methods provide quantitative and/or qualitative assessment of the significance of each technique. The measurement techniques lend themselves for widespread application in multi-phase flow imaging research and some for industrial-scale measurements due to their non-invasive nature.

1. INTRODUCTION

Multi-phase flows are widely used in industrial operations such as fluidized beds, bubble columns, slurry bubble columns, and solid–liquid and solid pneumatic conveying. They have been utilized extensively in the chemical, petrochemical, metallurgical, food, and pharmaceutical industries. To investigate multi-phase flow behavior, measurement techniques are vital for understanding and quantifying multi-phase system parameters. These techniques are classified generally into intrusive and non-intrusive based on the mechanism of acquiring measurement signals. In intrusive techniques, the measurement probe penetrates the wall of the process to acquire the desired signal from direct contact with the flow, which may perturb the physical flow, whereas non-intrusive techniques are based on remotely acquiring the measurement signal from sensors mounted away from the flow. In most case, these sensors are mounted at the periphery of the process walls internally or externally. In order to fully investigate different multi-phase flow behavior, a number of measurement techniques, both intrusive and non-intrusive, have been developed.

Intrusive probes that have been used to measure multi-phase flow systems include capacitance probe (e.g., Geldart and Kelsey, 1972; Gunn and Al Doori, 1985; Ho et al., 1983; Lanneau, 1960; Sharma et al., 2000; Shi et al., 1991; Werther and Molerus, 1973), optical fiber probe (e.g., Bayle et al., 2001; Cui and Chaouki, 2004; Du et al., 2003; Liu et al., 2003a, 2003b; Nakajima et al., 1991; Okhi and Shirai, 1976; Smith et al., 1999; Yasui and Johanson, 1958), endoscopic probe (e.g., Du et al., 2004a; Peters et al., 1983), and pressure transducer probe (e.g., Fan et al., 1981; Geldart and Xie, 1992; Gibilaro et al., 1988; Kang et al., 1967; Lirag and Littman, 1971; Sitnai, 1982). These techniques have been used intensively to measure gas–solid fluidized beds. However, intrusive probes pose unique challenges to their operation based on the modality of probe used.

For example, the capacitance probe is sensitive to electrostatic charges influenced by temperature and relative humidity, making it difficult to define the measuring volume. As for the optical probe, the measuring volume is not well defined and varies with the solid concentrations in the bed, introducing an error into the measured signal (Du et al., 2003). A reliable and precise calibration is essential in this case. Additionally, pressure probes can only provide local, averaged information inside a fluidized bed, making it difficult to trace the cause of pressure changes. For example, the bubble flow, bubble coalescence, and bubble breakup, bubble burst at the top surface, bubble formation at the distributor can all generate the pressure variations in the same bed. Moreover, it is evident that the pressure probe measurement interferes with the bubble flow behavior in fluidized beds. In this case, bubbles are vulnerable to break, accelerate, or elongate by the immersed probe (Rowe and Masson, 1981). Small probes are often used to minimize the interference with the flow. However, such probes can be easily damaged. Comprehensive reviews of principles and applications of intrusive techniques in gas–solid fluidized beds are provided by Yates and Simons (1994), Werther (1999), and Du et al. (2003).

Non-intrusive techniques, on the other hand, have the advantage of avoiding interference with the internal flow of a multi-phase flow system. The information provided by non-intrusive techniques is usually in the form of two-dimensional (2D) cross-sectional concentration profiles or 3D volume images. Non-intrusive techniques used to measure multi-phase flow systems include X-ray (e.g., Gilbertson et al., 1998; Hulme and Kantzas, 2004; Hubers et al., 2005; Kai et al., 2005; Kantzas and Kalogerakis, 1996; Rowe and Matsuno, 1971; Rowe and Partridge, 1965; Rowe and Yacono, 1976; Yates et al., 1994), γ-ray tomography (GRT) (e.g., Baumgarten and Pigford, 1960; Boyer and Fanget, 2002; Clough and Weimer, 1985; Orcutt and Carpenter, 1971; Patel et al., 2008; Schubert et al., 2008; Wang et al., 2001; Weimer et al., 1985; Wu et al., 2007), positron emission tomography (PET) (e.g., Dechsiri et al., 2005a, b; Hoffmann et al., 2005), radioactive particle tracking (RPT) (e.g., Larachi et al., 1997; Larachi and Chaouki, 2000), magnetic resonance imaging (MRI) (e.g., Fennell et al., 2005; Holland et al., 2009; Savelsberg et al., 2002), electrical resistance tomography (ERT) (e.g., Bennett and Williams, 2004; Dickin and Wang, 1996; Vilar et al., 2008; Williams et al., 1993), electrical capacitance tomography (ECT) (e.g., Du et al., 2003, 2005; Halow and Nicoletti, 1992; Ormiston et al., 1965; Wang et al., 1995) and electrical magnetic tomography (EMT) (e.g., Binns et al., 2001; Williams and Beck, 1995). Although such methods (ECT, ERT, EMT) tend to non-intrusive due consideration may need to be given to the influence secondary effects, such as any influence on the effect of electromagnetic fields on the materials and their response within the process. Other

sensing principle might also include dielectric spectroscopy, microwave, ultrasound, and various conventional and diffuse optical methods (Cullivan and Williams, 2005).

Although non-intrusive imaging techniques span a wide range of sensing modalities, this chapter will focus on ECT, ERT, and PET techniques in multi-phase flow measurements. The reconstruction techniques applied to ECT, ERT, and PET are similar to algorithms developed for computed tomography (CT) in the medical field. However, in processes applications, these techniques can be studied after being categorized as algebraic reconstruction techniques (ART) or optimization reconstruction techniques (ORT). In the first category, a set of algebraic equations are formed to model the response of the system to density variations in the imaging domain. The measured signal is then used to obtain a density map based on matrix manipulation to solve the set of independent equations. Whereas in the optimization techniques, a set of objective functions are optimized together to obtain the most likely image associated with the measured signal. The performance of each reconstruction approach is different when applied to different tomography modalities and is usually related to the level of non-linearity between the signal detected and the density distribution. For example, ECT and ERT are two electric-based imaging modalities where the density distribution is non-linearly related to the electric field distribution inside the imaging domain. Optimization techniques in these two examples provide better imaging results when compared to algebraic techniques. Further details on reconstruction techniques are provided in (Benton and Parker, 1997; Warsito and Fan, 2001a, b; Williams and Beck, 1995; Yang and Peng, 2003). Investigating different reconstruction algorithms is beyond the scope of this chapter, we focus here on the applications of ECT, ERT, and PET techniques in fluidized beds, bubble columns, slurry bubble columns, and gas–solid pneumatic conveying.

2. ELECTRICAL CAPACITANCE TOMOGRAPHY

2.1 Introduction

Imaging technologies provide an invaluable insight into the dynamics of a multi-phase flow system operation. Such systems include fluidized beds, bubble columns, slurry bubble columns, and gas–solid pneumatic conveyers. The real-time rendering potential of electrical-based imaging technologies, along with low construction cost, high safety, and suitability with different vessel sizes, led to an increased interest in capacitance-based imaging systems. These systems based on electrical capacitance sensors are considered prominent among other imaging modalities and

have been widely used to study the hydrodynamics of multi-phase flow systems (Warsito and Fan, 2001a, b, 2003).

2.2 Principle of ECT

An ECT system is composed of three basic components: (1) a capacitance sensor, (2) a data acquisition system, and (3) a computer system for reconstruction and viewing. Figure 1 is a sketch of the ECT system with all three components (Warsito and Fan, 2003). The capacitance sensor is made of n_e capacitance electrodes distributed around the wall of the process vessel. The n_e capacitance electrodes provide up to $n_e(n_e-1)/2$ combinations of independent capacitance measurements between the electrode pairs. The capacitance measurements are related to the local dielectric constant (permittivity) filling the process vessel between electrode pairs (Figure 2) (Warsito and Fan, 2001b). The relation between the electric potential and the permittivity distributions follows Poisson equation shown in Equation (1).

$$\varepsilon(x,y)\nabla^2\phi(x,y) + \nabla\varepsilon(x,y)\nabla\phi(x,y) = 0 \tag{1}$$

where $\varepsilon(x,y)$ is the dielectric constant (permittivity) distribution and $\phi(x,y)$ is the potential distribution for an electrode pair of the $n_e(n_e-1)/2$

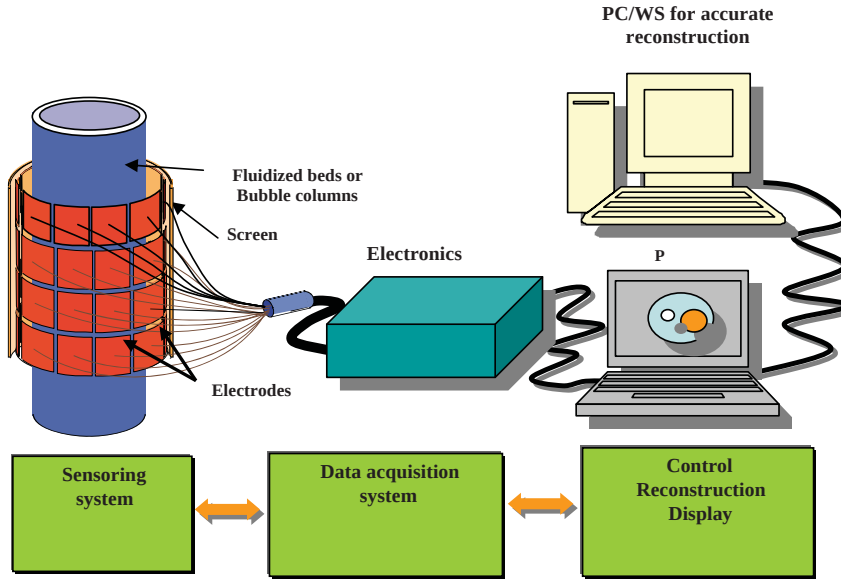

Figure 1 Sketch of the ECT system including sensor, data acquisition system, and computer for reconstruction (Warsito and Fan, 2003).

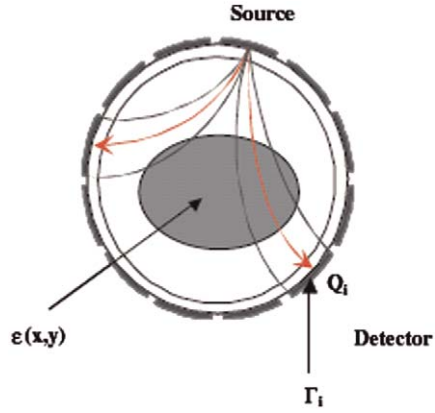

Figure 2 Principle of ECT capacitance measuring system (Warsito and Fan, 2001 b).

combinations. The accumulated charge on the detector electrode (Q_i) (Figure 2) is expressed in Equation (2)

$$Q_i = \oint_{\Gamma_i} \varepsilon(x,y)\nabla\phi \cdot \hat{n}dl \tag{2}$$

where Γ_i is a surface enclosing the detector electrode and $\hat{n}$ is the normal vector to Γ_i. The capacitance between the source and the detector electrodes for the ith electrode pair, C_i, is expressed in Equation (3).

$$C_i = \frac{Q_i}{\Delta V_i} = \frac{1}{\Delta V_i}\oint_{\Gamma_i} \varepsilon(x,y)\nabla\phi \cdot \hat{n}dl \tag{3}$$

From the above equation, the measured capacitance between the source and the detector electrodes of the electrode pair i is determined from the given dielectric constant (permittivity) distribution of the medium under investigation. The processes of finding the capacitance for a given permittivity distribution is referred to as the *forward problem*. On the other hand, the process of finding the permittivity distribution from a set of capacitance measurements is referred to as the *inverse problem*.

Various schemes have been applied to solve the forward problem of ECT for the visualization of multi-phase flow components. Forward solutions based on the sensitivity model (Huang et al., 1989; Xie et al., 1992) are the most widely used due to the simplicity and speed of applying this model. The simplest form of the sensitivity model is the single iteration *linear forward projection* (LFP) which is explained in Equation (4).

$$C = SG \tag{4}$$

where G represents the $M \times 1$ image vector (permittivity distribution in the imaging domain), C is the $N \times 1$ measured vector of capacitances

between the n_e electrodes pairs, and S is an $N \times M$ so-called sensitivity matrix. This matrix is constructed by solving Equation (3) usually by using computational methods or by experimental measurements. The basic idea of the sensitivity model is to assume that each permittivity pixel contributes linearly to the overall measured capacitance, and the forward problem can be reduced to a simple matrix multiplication.

Solving the inverse problem, on the other hand, is a higher level of complexity as the problem is often ill-posed and ill-conditioned. Various reconstruction techniques have been developed to solve the problem, and the most widely used is based on a single iteration *linear back projection* (LBP). Despite the simplicity of the LBP technique and its capability of providing real-time imaging, it suffers from severely blurred imaging, which led researchers to develop an iterative scheme of reconstructive algorithms (Yang and Peng, 2003). On the basis of iterative reconstruction, the error between the forward solution and the measured capacitance is reduced iteratively until reaching a preset error level. Iterative image reconstruction techniques (Yang and Peng, 2003) are mainly classified into ART and optimization techniques. Iterative linear back projection (ILBP) (Yang et al., 1999) is one of the most used ART. Iterative reconstruction techniques are generally described by Equation (5).

$$G^{k+1} = G^k + \alpha^k S^T \left(C - SG^k \right) \tag{5}$$

where G^k is the estimated permittivity vector in the kth iteration, α is a relaxation factor. The structures of α and the procedure to correct the estimated image vector (permittivity distribution) varies based on different ART.

However, due to the severity of the ill-posedness of the ECT inverse problem, iterative schemes often diverge if a limit on the number of iterations is not preset. In an attempt to provide better reconstruction results for quantitative imaging, researchers developed multi-objective optimization schemes for electrical tomography image reconstruction. One of the most prominent reconstruction techniques in this regard is the *neural network multi-criterion image reconstruction technique* (NN-MOIRT). The NN-MOIRT has been shown to provide better reconstructed image resolution, guaranteed convergence to a local minimum in the optimization process, and immunity to measurement noise (Warsito and Fan, 2001b). This reconstruction technique is even more valued when considering 3D volume reconstruction, as the inverse problem is severely ill-posed (Marashdeh et al., 2008; Warsito et al., 2007). NN-MOIRT is designed to optimize a set of objective functions that include the mean square error (MSE), entropy objective, and the smoothness functions as depicted in Equations (6–8), respectively. The entropy objective function is a measure of the information coded in the image. The smoothness

function is equivalent to a filter for eliminating measurement noise.

$$f_{mse}(G) = \frac{1}{2}\gamma_1 \|SG - C\|^2 \tag{6}$$

$$f_i(G) = \gamma_2 \sum_{j=1}^{N} G_j \ln(G_j) \tag{7}$$

$$f_s(G) = \frac{1}{2}\gamma_3 (G^T XG + G^T G) \tag{8}$$

In the above equations X is an $M \times M$ non-uniformity matrix and γ_1, γ_2,γ_3 are normalized constants between 0 and 1. Figure 3 shows the comparison of reconstruction results for a two-phase flow system from (a) noise-free data and (b) noise data using LBP, ILBP, SIRT, and NN-MOIRT techniques (Warsito and Fan 2001b). When there is no noise added, the ILBP, SIRT, and NN-MOIRT techniques provide relatively accurate reconstructed images, and the images consist the original permittivity distribution. LBP only provides a rough estimation of the original image. When noise is added, reconstructed images from LBP are worse, and images from ILBP and SIRT are not accurate enough compared to the original image. It is clear from this study that the NN-MOIRT technique is more effective in reconstructing an image and eliminating noise when compared to other widely used reconstruction techniques.

2.3 ECT applications

2.3.1 Circulating fluidized beds

ECT is used to image flow behaviors in circulating fluidized beds (CFB) models. The ECT imaging of choking in CFB is presented here. Choking is a complex phenomenon in gas–solid fluidization, where a sudden small change in gas or solid flow rate introduces a large change in the hydrodynamic behavior such as the pressure drop or solids holdup in the gas–solid flow (Du et al., 2004a, b). To fundamentally understand choking, it is important to observe the CFB operating variables during the choking transition from dilute to dense fluidization and the underlying mechanism. The initiation of choking, or the collapse of dilute suspension, introduces a sharp increase in the pressure drop in the vertical CFB riser. It has been deduced that only when the gas flow rate is lower than the transport velocity, U_{tr}, or the solids circulation rate is smaller than the transport solid circulation rate, $G_{s,tr}$, that the initiation of choking occurs with increasing solids circulation rate at a given gas velocity or with decreasing gas velocity at a given solids circulation rate in a vertical CFB riser. The qualitative and quantitative information

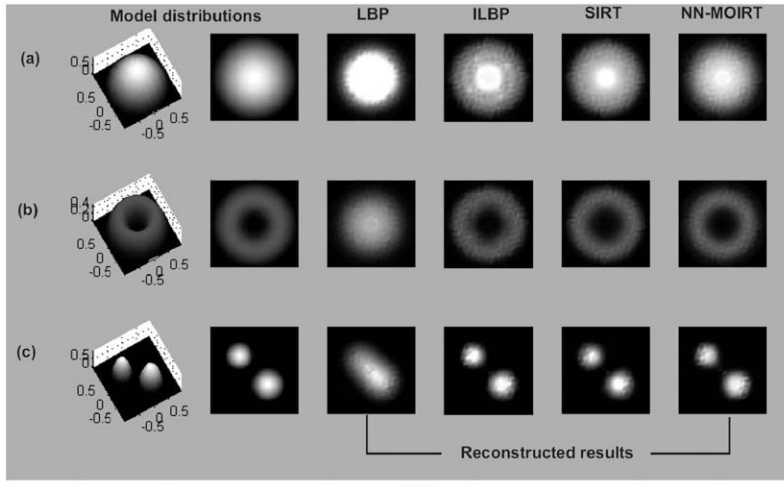

Figure 3 Comparison of reconstruction results for a two-phase flow system from (a) noise-free data and (b) noise data using LBP, ILBP, SIRT, and NN-MOIST techniques (Warsito and Fan, 2001b).

regarding microscopic and macroscopic flow structure of the gas–solid fluidization is needed to fully understand the choking mechanism. Pressure drop sensors and intrusive probes have been used to provide general information of the flow behavior. However, a measurement system capable of providing detailed information of the flow behavior during choking is required to fully understand the phenomena. In this

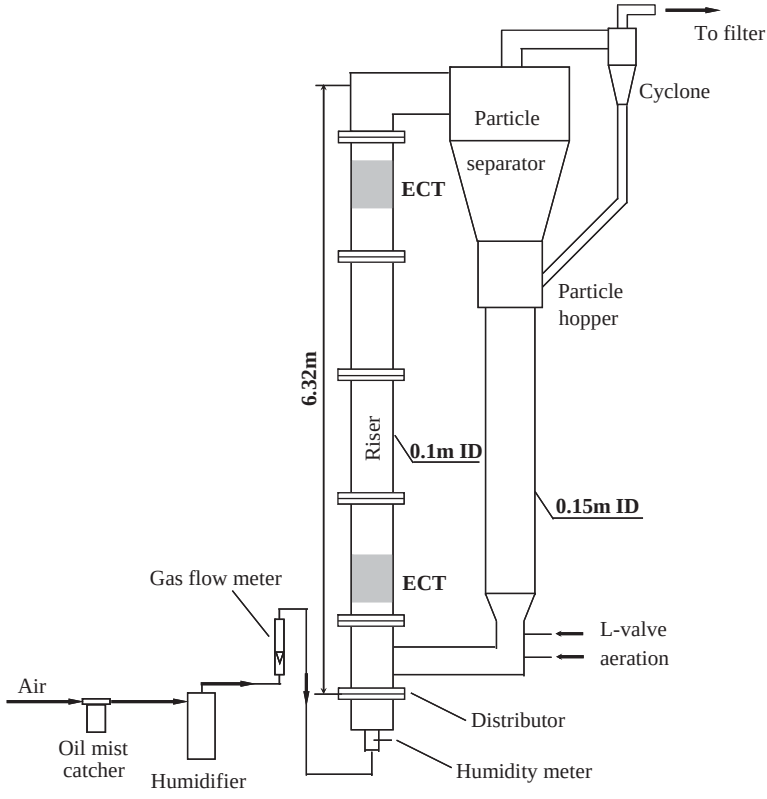

Figure 4 Sketch of a circulating fluidized bed (Du et al., 2004a).

regard, ECT is a reliable instrument for accurate, real-time imaging of multi-phase flow and can be applied for acquiring in-depth information of the flow during choking in CFB risers.

Figure 4 is the sketch of a circulating test fluidized bed (Du et al., 2004a). The CFB riser includes a 0.1-m ID riser with a height of 6.32 m, a separator and a secondary cyclone system, a large volume solids storage hopper, and an L-valve. FCC catalysts with a mean diameter of 60 μm and particle density of 1400 kg/m^3 are used as the fluidized particles in the CFB riser. ECT sensors are installed at both the lower and the upper position of the CFB riser. Quasi-3D flow structure of the CFB is provided after reconstruction of the capacitance signal from the ECT sensors using NN-MOIRT reconstruction algorithm developed by Warsito and Fan (2001b). Figure 5 is the Quasi-3D flow structures at lower part of a CFB riser (Du et al., 2004a). At that lower part of the CFB riser, a persistent dilute gas ring is clearly observed between the solid core and the solid ring near the wall with a low solid circulation rate $G_{s,tr}$ of 2.3 kg/m^{2}s and

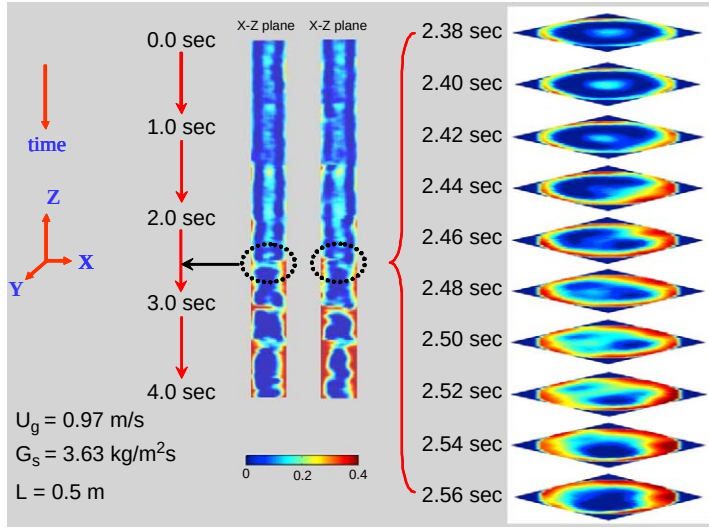

Figure 5 Quasi-3D flow structures for the choking transition at lower part of a CFB riser (Du et al., 2004a) (see Plate 9 in Color Plate Section at the end of this book).

a gas velocity U_g ($U_g < U_{tr}$)of 0.97 m/s, which is shown in the X-Z and Y-Z plan images between 0.0 sec and 2.3 sec in the left side of Figure 5. A large dilute gas core occurs in the central region and the size of the solid ring near the wall increases solid circulation rate $G_{s,tr}$ of 3.63 kg/m^{2}s at same gas velocity U_g of 0.97 m/s. This occurrence is shown in the left side of Figure 5 in the X-Z and Y-Z plane images between 2.6 sec and 4.0 sec. An abrupt flow structure change, or choking transition, to dense-phase fluidization occurs when the solid circulation rate undergoes a step increase from 2.3 to 3.63 kg/m^{2}s, which is also shown in the X-Z and Y-Z plane images around time 2.4 sec in Figure 5. The detailed flow structure variation and choking transition in the CFB riser is provided in the X-Y plane images in the right side of Figure 5. Before the choking transition, the solid concentration in the core region and the solid ring near the wall measured by ECT is about 0.15 and 0.25, respectively. During the choking transition, solids in the core region move toward the wall. Subsequently, solids keep moving between the core region and the wall region in the riser, which is described as a dynamic process, or choking transition, until the new structure forms. After the choking transition, a dilute gas core region in the center of the riser and a large dense solids ring near the wall of the riser are formed. The concentration in the dense solid ring near the wall measured by the ECT is about 0.4. The ECT provided a real-time quasi-3D cross-sectional flow structure of the circulating fluidized bed. It also helped reveal flow conditions before and

after the choking as well as the underlying mechanism of the choking formation.

2.3.2 Pneumatic solid conveying

Transportation of solids is commonly required in many solid processing systems. Among numerous solid transportation techniques, pneumatic conveying is widely used because of its advantages in requiring low routine operation, maintenance, and low labor costs. Additionally, this technique is appealing because of its characteristics of being dust free and flexible in routing and spacing (Fan and Zhu, 1998; Ostrowski et al., 1999). However, the pneumatic solid conveying system consumes more power than other bulk solid transportation systems. It also introduces high wearing and abrasive effects on the solids due to their high collision velocity. The pneumatic solid conveying system is classified based on the following criteria: (1) the angle of the inclination of the pipelines; (2) operational conditions; (3) flow characteristics. A fundamental understanding of the transport phenomena associated with the pneumatic solid conveying system is of great importance to design and optimize the transportation systems. The ECT is considered here a robust, reliable, and non-intrusive technique for accurate, real-time imaging of gas–solid flows in the pneumatic solid conveying system. The qualitative and quantitative information of the flow structures in this system are obtained by using the ECT. For example, ECT was used to study the horizontal pneumatic solids conveying test plant behaviors for the industrial-scale pneumatic conveyors (McKee et al., 1995a). Eight electrodes in this case were used to obtain a total of 28 independent capacitances for each measurement. The 2D reconstruction images calculated from the dielectric constant (permittivity) distribution show the solid distribution of the test cross-sections of the pipe. Figure 6 depicts the solid distribution of the cross-sections at upstream (0.88 m away from the solids feeder) and downstream (4.08m away from the feeder) of a horizontal pipe with different solids loading in a pneumatic solids conveying system. Acetal resin pellets with a diameter of 2.85mm, a bulk density of 879 kg/m^3, a particle density of 1350 kg/m^3, and different solids loading factors (10:1; 7:1; 4:1; 1:1) are used for the test. At high solid loading rate (10:1, 7:1) and an air conveying velocity of 28 cm/s, solid deposition is observed from ECT results both at the upstream and downstream of the horizontal pipe. At low solid loading rate (4:1, 1:1) with the same air conveying velocity, the ECT at the downstream of the horizontal pipe shows the particle conveying flow fully suspended with no solid deposition observed (McKee et al., 1995a). These results from a solid conveying system show that the ECT is capable of providing online cross-sections of solid concentration in pneumatic solid conveying systems. The methods were further refined to

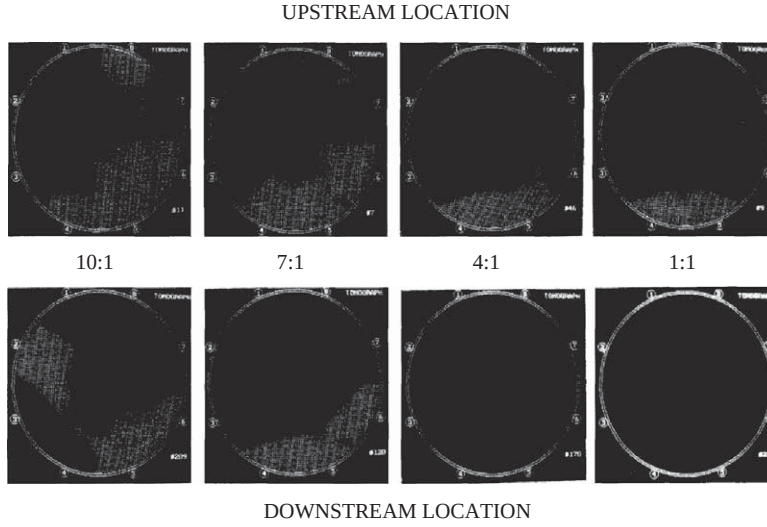

Figure 6 Solid distributions at upstream and downstream of a horizontal pipe with different solids loading (McKee et al., 1995a).

demonstrate applications for real-time control of pneumatic conveying systems based on flow regime characterization and recognition (Ostrowski et al., 2000). This also provided significant detail that could be utilized for direct visualization of the shape of powder slugs and the estimation of velocity profiles within the conveyor (Williams, 2005). Some of the data handling and modeling methods derived are also applicable to other electrical tomographic methods.

2.3.3 Hydrodynamic behaviors in bubble and slurry bubble columns

Gas–liquid bubble columns and gas–liquid–solid slurry bubble columns are widely used in the chemical and petrochemical industries for processes such as methanol synthesis, coal liquefaction, Fischer–Tropsch synthesis and separation methods such as solvent extraction and particle/gas flotation. The hydrodynamic behavior of gas–liquid bubble columns and gas–liquid–solid slurry bubble columns are of great importance for the design and scale-up of reactors. Although the hydrodynamics of the bubble and slurry bubble columns has been a subject of intensive research through experiments and computations, the flow structure quantification of complex multi-phase flows are still not well understood, especially in the three-dimensional region. In bubble and slurry bubble columns, the presence of gas bubbles plays an important role to induce appreciable liquid/solids mixing as well as mass transfer. The flows within these systems are divided into two

regimes, homogeneous and heterogeneous. In the homogenous regime, the variation of the bubble size is small and no coalescence of bubbles occurs. In the heterogeneous regime, substantial coalescence and breakup of bubbles make the flow very complex and the variation of the bubble size extremely large. The qualitative and quantitative information regarding flow structures of the bubble and slurry bubble columns is required for understanding the heat and mass transfer behaviors within these systems. Among available tomography technologies, ECT is one of the most promising techniques for dynamic flow imaging measurements. ECT provides real-time qualitative and quantitative cross-sectional imaging data of the multi-phase flow behaviors in bubble and slurry bubble columns. Some examples of measurements mapping flow regimes and detailed microstructure development were achieved using ECT (Bennett et al., 1999). For aqueous-continuous fluidized systems, it may be possible to perform measurements that can be probed using ERT (e.g., Jin et al., 2006). Dielectric methods based on ECT are normally better for systems at high gas voidage. This is because the presence of gas bubbles (infinite resistance) can cause spurious outcomes using current injection methods, although some remedies have been proposed which will be discussed later.

An improvement to the ECT system utilizes capacitance sensors to provide direct 3D imaging in what is known as electrical capacitance volume tomography (ECVT). This innovative approach was used to investigate the hydrodynamic behaviors in gas–liquid bubble columns and gas–liquid–solid slurry bubble columns (Warsito and Fan, 2005). The 3D real-time gas holdup distribution, the transient phenomena in the entrance region of gas–liquid bubble columns and gas–liquid–solid slurry bubble columns, and the 3D bubble plume spiral motion and liquid vortex dynamics were investigated using the 3D ECVT sensor and the 3D-NN-MOIRT reconstruction technique. Figure 7 depicts a design of an ECVT sensor that reveals its 3D features (Warsito and Fan, 2005). The electrical potential distribution between the electrode pairs is also depicted in the figure. Twelve capacitance electrodes were arranged in two planes. The capacitances between the electrode pairs of different layers (top-right) provided the feasibility for measuring the capacitance in the 3D volume of the test region. A related 3D sensitivity model was established to solve the volume image reconstruction problem which provided a $20 \times 20 \times 20$ voxels image (bottom-left). Figure 8 is a 3D real-time volume tomography image of gas–liquid flow in a bubble column (Warsito and Fan, 2005). The spatial and time resolution is $5 \times 5 \times 8\,\text{mm}^3$ and 12.5 ms, respectively. The X-Z, Y-Z, and X-Y planes to render the images are defined by the coordinate system in the bottom-right of the figure. The phase concentration (holdup) of the multi-phase system is calculated from the permittivity distribution of the flow volume

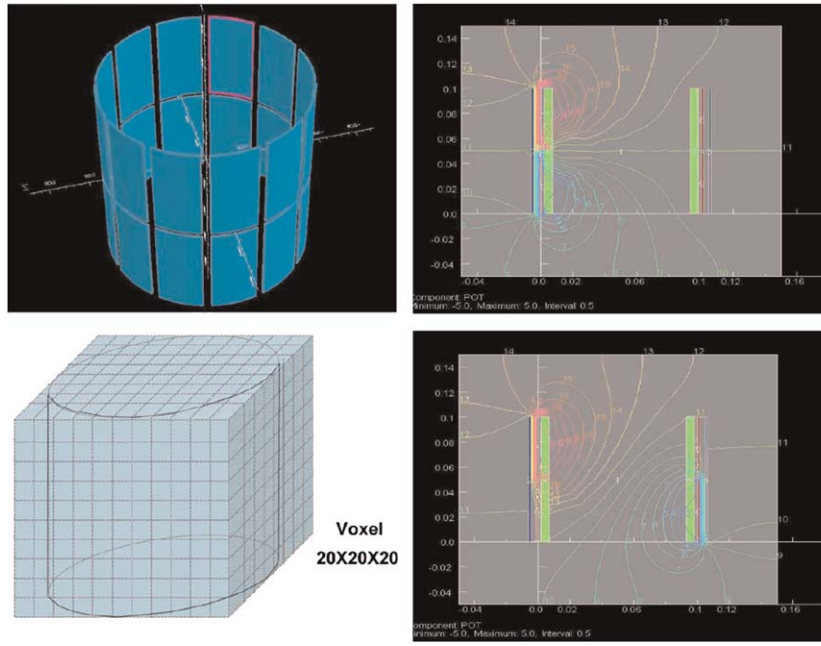

Figure 7 Three-dimensional ECVT sensor configuration and electrical potential distribution (Warsito and Fan, 2005) (see Plate 10 in Color Plate Section at the end of this book).

reconstructed by ECVT. The blue and red colors represent low and high gas holdup, respectively. The top-left two pictures of Figure 8 show a snapshot of the bubble gas holdup distributions in the X-Z and Y-Z planes, respectively. The bottom-left two pictures of the figure show the 3D perspective volume image and 3D isosurface image of the bubble swarm within the bubble column. The 3D isosurface image displays the bubble swarm boundary with a cut-off boundary value of 10%. The cut-off boundary has no strict criterion. It is arbitrarily used to distinguish boundary between the fast moving bubble swarm and the surrounding liquid flow as well as to show the motion of the bubble swarm clearly. A photograph of the gas–liquid flow in the bubble column with the same condition taken by a high-speed digital video camera system is displayed on the top-right image of the figure. It is compared to the X-Z plane, Y-Z plane, 3D volume, and 3D isosurface images. Two main flow regimes, a fast bubble flow regime with a fast motion and high gas hold up, and a vertical-spiral liquid flow regime with a slow motion and low gas holdup, are observed in the gas–liquid bubble columns. The ECVT images clearly show that the fast bubble flow regime, or the spiral bubble plume flow regime, has circular motion when it is rising. This observation is consistent with those observed by Chen et al. (1994).

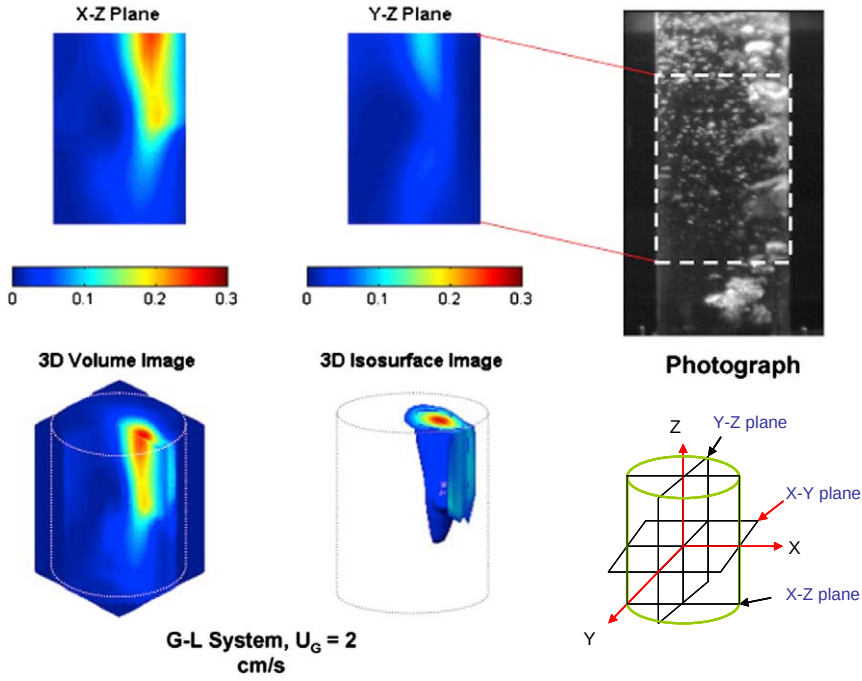

Figure 8 Three-dimensional ECVT images of gas–liquid flow in a bubble column (Warsito and Fan, 2005) (see Plate 11 in Color Plate Section at the end of this book).

Although ECVT is a promising non-intrusive technique, this system is limited to measuring bubbles greater than the voxel resolution. A bubble smaller than the voxel resolution cannot be measured by the ECVT. A potential solution to this issue is to increase the number of sensor electrodes and modify the related sensitivity which could increase the resolution to track the smaller, single bubble.

The unique capability of ECVT in viewing 3D real-time images of multi-phase flow systems is best demonstrated in the example of horizontal gas penetration in a gas–solid fluidized bed reported in Wang et al. (2008). A gas–solid fluidized bed with a 0.3 m ID and a total bed height of 2.4 m and FCC particles with a mean diameter of 60 μm and a particle density of 1400 kg/m^3 are used in this example. A horizontal tube is mounted on the wall of the testing section of the fluidized bed, 0.3 m above the distributor to provide horizontal jets in the fluidized bed. The testing region of the fluidized bed with the horizontal side injection is covered with the ECVT sensor. The sensor consists of three layers with four electrodes in each layer. Each electrode has a rectangular plate shape. The edges of the two side-by-side electrodes in the middle layer are modified to accommodate the penetration tube. Figure 9a shows a 3D

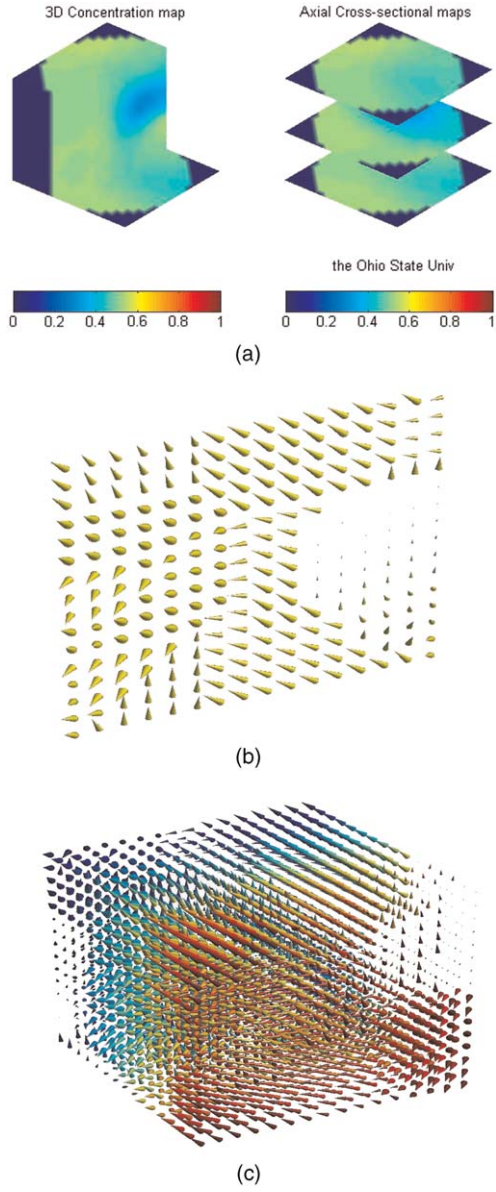

Figure 9 (a) Three-dimensional view of 3D solid concentration with a horizontal gas jet in the fluidized bed; (b) 3D voxel-volume-averaged solid phase velocity vector map in the Y-Z plane of the fluidized bed; (c) 3D voxel-volume-averaged solid phase vector map (Wang et al., 2008) (see Plate 12 in Color Plate Section at the end of this book).

view of 3D solid concentration with a horizontal gas jet in the fluidized bed. Blue and red colors represent low and high solid concentrations in the fluidized bed, respectively. The 3D shape of the horizontal jet and its development in the gas–solid fluidized bed are viewed by ECVT. The voxel-volume-averaged phase velocity vector field of the gas–solid fluidized bed with the horizontal jet is obtained from quantitative ECVT images. Figure 9(b) shows the 3D voxel-volume-averaged solid phase velocity vector in the Y-Z plane (Y: the direction of the horizontal jet; Z: vertical direction relative to the jet) of the fluidized bed. Figure 9(c) shows the 3D voxel-volume-averaged solid phase velocity vector in the whole ECVT test region of the gas–solid fluidized bed. In this example, quantitative ECVT provides the maximum horizontal jet penetration length, maximum horizontal jet width, and the voxel–volume-averaged phase velocity vector. It is generally perceived that increasing the electrode sensor numbers and acquisition channel numbers for the ECVT system would yield images of higher resolution. A 32-channel ECVT system providing real-time 3D images has been demonstrated recently for such multi-phase flow systems for a high resolution effect (Wang et al., 2008). Figure 10 depicts such 32-channel system for this demonstration. It is seen that the sensor used in this figure is of four layers of shifted planes, with eight electrodes in each layer. All the 32 channels in all 4 planes are used to obtain each image frame. Figure 10b shows a multi-phase flow column with 32-channel ECVT sensors mounted on the wall along with acquisition hardware. The column is of a 0.3 m ID and a total height of 0.6 m. The ECVT sensor is connected to a 32-channel acquisition box. A laptop is used to control the acquisition hardware and perform image reconstruction. In the images shown in Figure 10c, imaging is conducted with liquid used in the column.

3. ELECTRICAL RESISTANCE TOMOGRAPHY

3.1 Introduction

Electrical resistance tomography is a technique used for medical and industrial applications. It is based on injecting current into the reactor domain of interest and measuring conductivity changes that can be used to reconstruct a conductivity map of the electrode plane region. The variation in electrical conductivity of different materials can be used to interpret the ERT images. Current injection measurements are often made at a single frequency using a sinusoidal or pulsed waveform. But multiple frequencies can also be utilized through spectroscopic methods. This enables both ''real'' and ''imaginary'' components of the electrical signals to be analyzed and in effect giving an impedance map. ERT is the

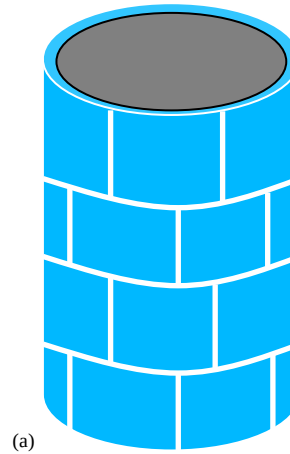

(a)

(b)

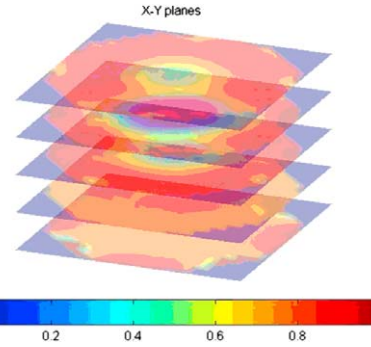

(c)

Figure 10 (a) Configuration of the 32-channel ECVT sensor; (b) fluidization system mounted with the 32-channel ECVT acquisition system; (c) liquid holdup image obtained by the 32-channel ECVT system (Wang et al., 2008) (see Plate 13 in Color Plate Section at the end of this book).

real component of this map and is most widely used. However, full electrical impedance tomography (EIT) is also possible from which real (resistivity) and imaginary (dielectric) data can be abstracted (West et al., 2002). ERT exhibits the same advantages of other electrical imaging modalities except that it generally requires an invasive insertion of probes to inject current. In industrial applications, ERT offers complementary and relatively low-cost measurements in multi-phase flow applications such as solid/liquid and miscible liquid/liquid mixing, hydrocyclone flow visualization, high-speed flow imaging in slurry conveying system, and the spatial concentration of the dispersed phases in pipelines, separators, and reactors (Dickin and Wang, 1996; Fangary et al., 1998; George et al., 2000; Lucas et al., 1999; Primrose, 2008; Vilar et al., 2008; Williams et al., 1993; Williams et al., 1999). ERT uses conductive sensors on the wall of the process vessel to inject current and then sense voltage differences from which the conductivity of the electrolyte inside the process vessel can be measured. Like other electrical methods, various approaches can be used to analyze the data, which are discussed below. Although there is much attention given to reconstructions using algorithms to interpret the internal distribution of resistivity in the process vessel, other methods are also extremely valuable and will be considered below. Since ERT is a soft field tomography modality, similar to other electrical tomography modalities, many of the reconstruction techniques presented in the previous section for ECT can be used for ERT as well. The distribution of the resistivity provides quantitative imaging of the phase distribution in the process vessel. ERT has been widely used to study the hydrodynamics of conductive multi-phase flows in the multi-phase systems.

3.2 Principles of ERT

An ERT system is built on a sensor, a data acquisition system, and some form of interpretation facility, often an image reconstruction algorithm, which are three key elements of a tomography system (Wang et al., 1994). Figure 11a is a sketch of the ERT system with all its components. The sensor electrodes are made of conductive materials, usually with a relative conductivity much higher than the electrolyte, penetrating the process vessel where one electrode injects current in the electrolyte whereas the rest act as receivers. The sensor shown in Figure 11a has four layers of electrodes with equal intervals in height on the axis direction of the process vessel. Each layer has an equal number of electrodes with equal intervals around the process vessel. The sensor arrays provide resistivity measurement between the electrodes both in the layer and between different layers. The data acquisition system is designed to provide resistivity measurements from measured currents at the

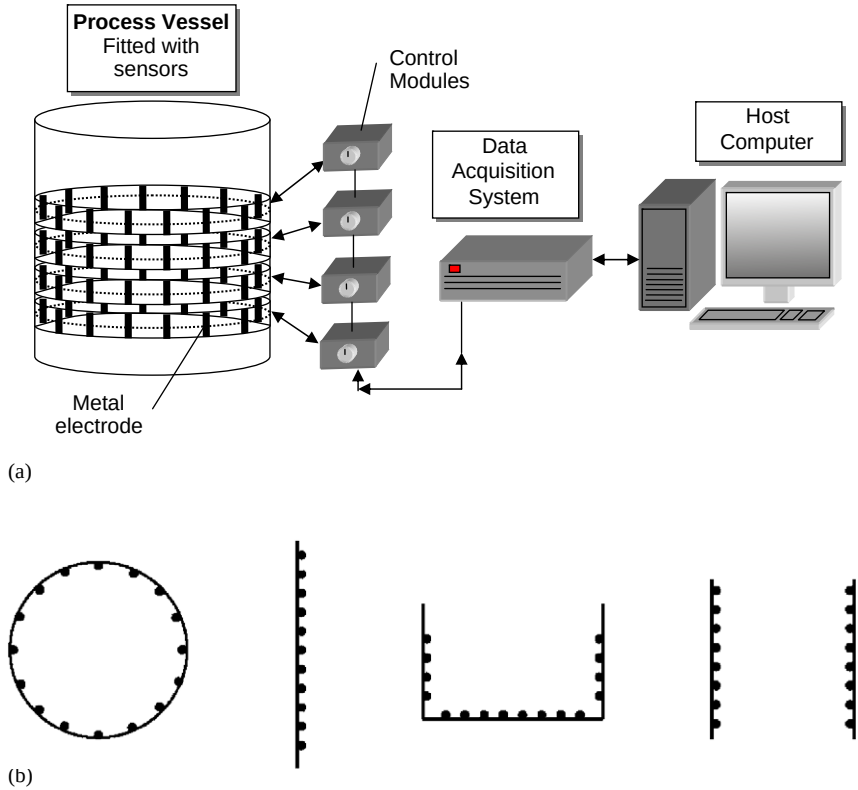

Figure 11 (a) Sketch of the ERT system including a multi-layer circular sensor array, data acquisition system, and computer for reconstruction and (b) various electrode arrangements in form of circular, probe, channel, and dual probe arrays.

receiving electrodes. Different designs are usually implemented in distributing the electrodes for proper 3D resistivity measurements (Dickin and Wang, 1996).

The objective of the sensor is the detection of differences of concentration in the multi-phase flow that is sensed through detecting changes in local electrical properties of the different phases. In ERT, the applied source is electrical current 0–75 mA between 75–500 kHz, the voltage is sensed, and the electrical property obtained is the conductivity (mS/cm). The change of the electrical properties in the multi-phase flow is sensed by the sensor arrays (Figure 11a). In addition a spare electrode, referred to as the ground electrode, positioned away from the measurement electrodes but in electrical contact with the internal fluid is required to ensure all voltage measurements are fixed against a common ground source. The different configurations of the electrodes depend on

the process vessel to be measured. The electrodes are normally located equi-distantly around inner cross-sectional circumference of pipe or process system (Figure 11b). The electrodes are made of metals (platinum, silver palladium, etc.); stainless steel is preferred for its resistance to chemical attack. There are five main strategies employed in EIT depending on the injection of current and voltage measurement, shown in Figure 12:

1. Adjacent: In this strategy current is applied through two neighboring electrodes and the voltages measured from successive pairs of neighboring electrodes (Figure 12a). Current is then applied through the next pair of electrodes and the voltage measurements repeated. The adjacent measurement strategy yields N^2 measurements, where N is the number of electrodes. Furthermore, to avoid the effects from electrode/electrolyte contact impedance problems, the voltage is not measured at a current-injecting electrode so the total number of independent measurements is $N(N-3)/2$. The main shortcoming of the adjacent strategy is that it has a non-uniform current distribution since most of the current travels near the peripheral electrodes. Therefore, the current density at the centre of the vessel is relatively low which makes the strategy very sensitive to measurement error and noise (Hua et al., 1993). However, the strategy requires minimal hardware to implement and image reconstruction which is the main advantage.
2. Opposite: In this strategy current is applied through diametrically opposite electrodes (Figure 12b. The voltage reference is the electrode adjacent to the current-injecting electrode. Thus, for a particular pair of current-injecting electrodes, the voltages are measured with respect to the reference at all the electrodes except the current-injecting ones. The next data set is obtained by switching the current to the next pair of opposite electrodes in the clockwise direction and the voltage reference electrode is changed accordingly. The voltages are again measured using the same procedure and the whole procedure is repeated. Compared with the adjacent strategy, the

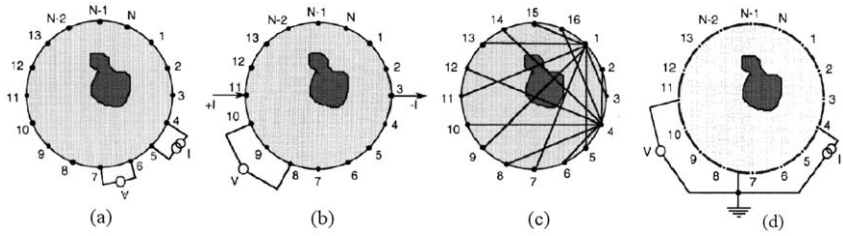

Figure 12 Common electrical excitation strategies for ERT measurement (adapted from Wang, 2002).

opposite strategy is less sensitive to conductivity changes at the boundary since most of the current flows through the central part of the region. However, it suffers from a serious disadvantage: for the same number of electrodes N, the number of independent measurements is less than for the adjacent strategy. Breckon and Piddcock (1987) showed that, for the opposite strategy, the number of independent measurements is given by $N/4N/2–1$).

3. Diagonal: In this strategy, currents are injected between electrodes separated by large dimensions (Figure 12c. The outcome, with respect to the adjacent strategy, is a more uniform current distribution in the region being imaged. For a 16-electrode tomography measurement, the data collection procedure is as follows: electrode 1 is fixed as a current reference and electrode 2 as the voltage reference; current is then applied successively to electrodes 3, 5, till 15. For each of these current pairs, the voltages from all electrodes except the current electrodes are measured with respect to electrode 2. The current reference is then changed to electrode 4 and the voltage reference to electrode 3 and current applied through electrodes 6, 8, till 16 and 2. As before, the voltage is measured on all other electrodes except the current-injecting ones. Thus, for each pair of current electrodes, 13 voltage measurements are obtained and seven different current electrode pairs are selected to give $7 \times 13 = 91$ data points. A further 91 points can be obtained by changing the voltage and current reference. Therefore, a 16-electrode system yields a maximum of 182 data points out of which only 104 are independent. The diagonal strategy does not yield a high sensitivity in the periphery compared with the adjacent method. However, it has better sensitivity over the entire region and is not as sensitive to measurement error and thus produces a better quality image (Hua et al., 1993).
4. Conducting boundary: The conducting boundary strategy was devised by Wang (1994) as a measurement strategy for use on process vessels and pipelines with electrically conducting boundaries (Figure 12d). As opposed to the preceding four-electrode measurement strategies, the conducting boundary strategy employs only two electrodes. The relatively large surface area of the conducting boundary is employed as the current sink to reduce the common-mode voltage across the measurement electrodes. Consequently, neither common-mode feedback nor earthed (load) floating measurement techniques are necessary in this strategy. The earthed conducting boundary also acts as a shield, reducing effects of electromagnetic interference. The conducting boundary strategy has a significantly lower common-mode voltage component than does the adjacent electrodes strategy. Wang (1994) reported it to be 800

times smaller for the conducting boundary strategy. Conversely, the amplitude of the measured voltages for identically shaped process vessels was approximately factor of 7 lower for the conducting boundary strategy in comparison with the adjacent strategy sensitivity is similar to that of the adjacent strategy.

5. Simultaneous current injection: Pioneering work based on medical electrical imaging used simultaneous current injection and voltage measurements, for example, the adaptive current tomographic system (ACT4) at Renslaaer group (Ross, 2003; Saulnier et al., 2006). It is a high-speed, high-precision, multi-frequency, multi-channel instrument, able to support up to 72 channels. The instrument is able to apply either voltage or currents to all the electrodes simultaneously and respectively measure the resulting currents or voltages. It can also control both the phase and the amplitude of the voltage or current excitation. Such a system can be configured to support 60 electrodes in two 5×6 radiolucent array and each electrode is driven by a 16-bit precision voltage source and has a circuit for measuring the resulting current and voltage. These circuits are digitally controlled to produce and measure signals at 5–1000 kHz. The magnitude and phase of each source are controlled independently. Each source, and each voltage and current measurement, is calibrated to a common standard reference (Saulnier et al., 2006). During each measurement, 59 orthonormal excitation patterns are used to maximize distinguishability and applications have focused on different medical flows, for example, pulmonary function (Kim et al., 2007).

The mathematical model of the ERT sensor electrodes is described in detail by Somersalo et al., (1992) and Kaipio et al. (2005), and principles of description are similar in many respects to those described earlier for ECT. The data measured using the EIT electrodes is transformed and analyzed by a data acquisition system. The analysis of the raw data enables to convert it into variables that describe the process to be measured. Different alternatives can be considered in the analysis of the data and some specifically for multi-phase systems. First, the use of raw measurements for statistical analysis to observe trends or for obtaining different statistical correlations. Second, the application of a process-based model using raw data as input. The distribution of concentration of the multi-phase flow is obtained by a model based on the characteristic parameters of the process (West et al., 2000). Also use of statistical methods such as Markov chain Monte Carlo (MCMC) based on prior information about the process have been successfully applied to reconstruct the images (West et al., 2004). Third, conversion of the raw data into images using a reconstruction algorithm. For ERT, for example,

the application of different algorithms such as LBP, Newton–Raphson method (NRM), sensitivity conjugate gradients (SCG) enables to obtain a group of images that show an estimation of the distribution of concentration of the multi-phase flow in the process (Wang, 2002; Xie, 1995). The mapping of the distribution of concentration enables the calculation of the parameters of the fluid such as the concentration and the velocity profiles. The reconstruction processes have their own limitations and require careful use to avoid misinterpretation.

The reconstruction of the images is independent of the parameters of a specific process; it is based entirely on the results obtained from the measurement and the image reconstruction algorithm. The choice of image reconstruction algorithm is a trade-off between accuracy of image and time required for reconstruction. Several image reconstruction algorithms have been developed to suit different tomography applications (Xie, 1995). There has been a demand for fast image reconstruction algorithms that can be used for the real-time imaging of fast-moving processes. Therefore, much effort has been focused on the development of image reconstruction algorithms, both non-iterative and iterative for ERT. A comprehensive comparison between image reconstruction algorithms was reported by Yorkey et al. (1987a). In particular the most employed techniques of reconstruction in ERT are filtered back-projection between equipotent lines (Barber, 1990); back projection using sensitivity coefficient (Kotre, 1989); perturbation method (Yorkey et al., 1987b); double-constraint method (Wexler et al., 1985); Newton–Raphson method (Abdullah 1993) and the SCG method (Wang, 2002).

In summary, a linearization of the forward problem follows the same concept discussed in ECT as both systems rely on the electric property distribution. The forward problem can be written in a matrix expression as in Equation (9).

$$Y \cdot v = c \tag{9}$$

where Y is a global admittance matrix (George and Liu, 1995), v is a vector representing the potentials of the mesh-node point, c is a vector representing the boundary current. Several back-projection algorithms and sensitivity coefficient methods (Barber et al., 1983; Breckon and Pidcock, 1987; Kotre, 1994) are developed for the qualitative reconstruction showing the changes of resistivity to the original reference distribution. Different quantitative algorithms (Abdullah, 1993; Loh, 1994; Yorkey, 1986) are also developed to provide the real values of the resistivity distribution on the pixels within the pixel vessel. ERT reconstruction algorithms are very similar to ECT reconstruction as the field distribution in both systems is governed by similar equations. A major practical difference however is the necessity to use corrections for the conducting boundary effects (Wang et al., 2005).

3.3 ERT applications

3.3.1 Hydrocyclone flow visualization and comparison with computational fluid dynamics

A hydrocyclone is a device to separate solids/particles from liquid from a suspension or to separate liquids of different density in fluid mixtures by means of difference in size or density (Cullivan and Williams, 2003). The hydrocyclone is widely used in industry such as separation of oil from water; separation of sand, staples, plastic particles from pulp, and paper mills; and separation of metal particles from cooling liquid in metal working. Figure 13 is a sketch of a hydrocyclone configuration and the flow structure in the unit. It consists of a cylindrical section with a tangential inlet at the top to feed the slurry suspension or liquid mixtures, a conical base for the separation, and two exits. One exit is at the bottom for underflow with the denser fraction, whereas the other is at the top for overflow with the lighter liquid fraction. The tangential inlet generates high swirl of the slurry suspension or liquid mixtures. Because of centrifugal force, the larger particles are thrown against the wall and move to the underflow. On the other hand, small particles, or lighter liquid, are dragged inwards to the overflow. The mechanisms of separation and models of fluid flow in hydrocyclone separators have been studied (Chocha et al., 1998; Dyakowski and Williams, 1998) but are still not well understood because of their complex high swirl and varying turbulence conditions, the presence of an interface inside the separator, and the requirement for online measurement data for the model development (Williams et al., 1999). Non-intrusive measurements such as ERT and computational fluid dynamics (CFD) are effective techniques to understand the internal flow of the hydrocyclone separator. Figure 14 is the ERT/EIT reconstructed image of the hydrocyclone cross-section compared to ultrasound tomography (UST) (Cullivan and Williams, 2003). Eight parametrically reconstructed sections are obtained in the conical base of the hydrocyclone. The light and dark colors represent

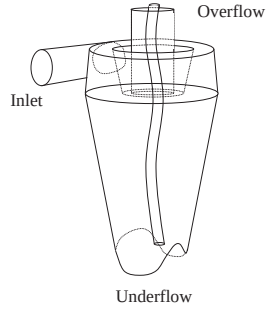

Figure 13 Sketch of the hydrocyclone flow structure.

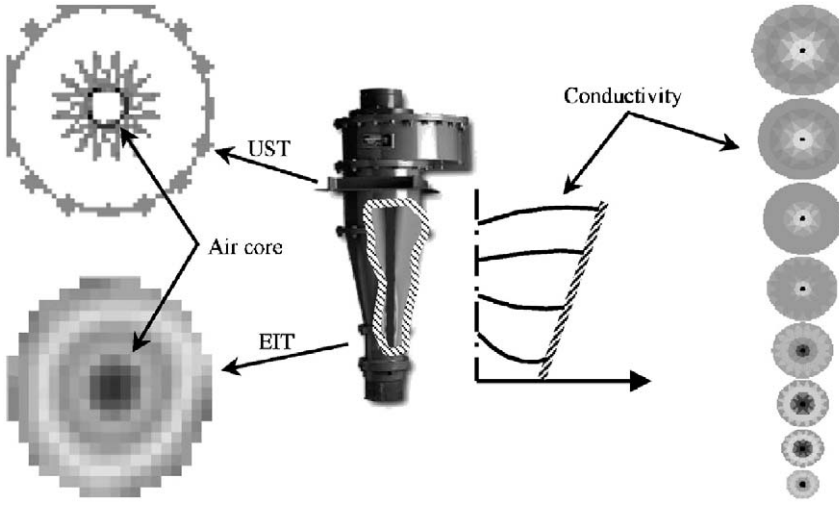

Figure 14 ERT tomographic image of the hydrocyclone cross section and the comparison with UST (Cullivan and Williams, 2003).

high and low conductivity material in the images, respectively. An air cone shape which has low conductivity is clearly shown as a dark region in the conical chamber of the hydrocyclone. The air cone shape obtained from ERT and that from the UST (top-left of Figure 14) are consistent with each other. ERT hydrocyclone measurements are solid validation for the CFD results on hydrocyclone simulations. Figure 15 is the positive axial-velocity contours in the hydrocyclone (Cullivan et al., 2004). The central axial-velocity is positive toward the underflows and an air-core is developed. ERT and CFD results show good agreement for the flow structure in the hydrocyclone.

3.3.2 High-speed flow imaging in slurry conveying

Hydraulic conveying systems use fluid to transport solid particles in pipes over long distance and is widely applied in chemical processes such as coal and mineral processing, oil drilling, pharmaceutical, and food industries (Laskovski et al., 2007; Lim, 2007; Yin and Wang, 2003). The solids concentration, size, density, distribution, velocity, and destabilization of the suspended solids are yet to be understood in the opaque and flowing slurry conveying system. Understanding the suspended solid flow behaviors and the solid distribution in hydraulic conveying systems is of great importance for the optimization and design of the conveyor, pressure drop estimation in the conveying pipe, and operations at maximum solids concentration (Fangary et al., 1998). ERT is being used to obtain conductivity maps across a slice of the conveying

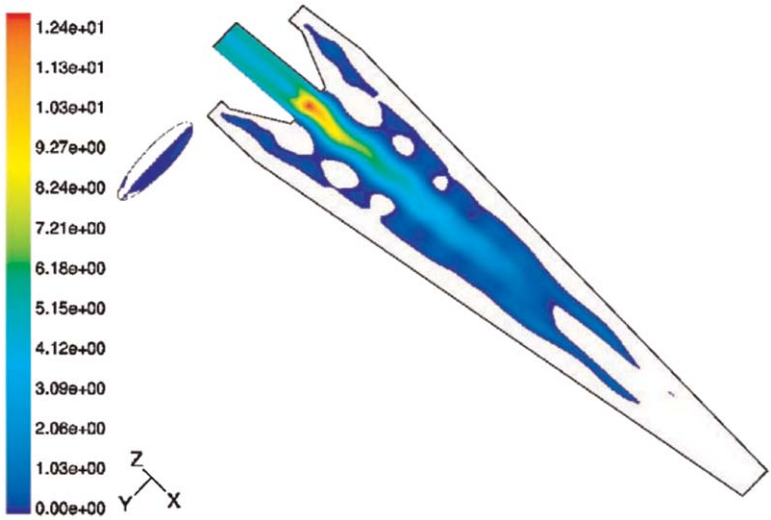

Figure 15 Axial velocity contours in hydrocyclone (Cullivan et al., 2004) (see Plate 14 in Color Plate Section at the end of this book).

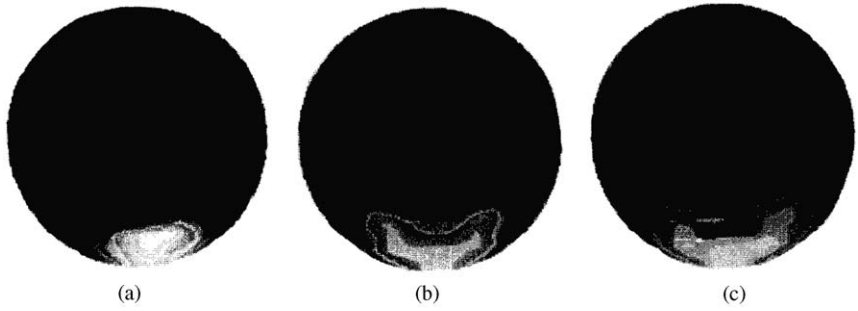

Figure 16 Tomographic images of three different deposit thicknesses in slurry conveying system (Fangary et al., 1998).

pipe to investigate the solid concentration and transport behaviors in the opaque and flowing slurry conveying system.

The images in Figure 16 represent the locations of the deposit-slurry interface for three different deposit thicknesses (13 mm, 31 mm, and 38 mm) in a hydraulic conveying system using ERT (Fangary et al., 1998). The fluid media is an electrolyte of 2.1 mS/cm and the working solids are spherical glass beads with a diameter of 5 mm. The surface of the deposit estimated from ERT images is higher than the actual sediment height. Nevertheless, they are consistent with each other. The results show that ERT is a useful tool in capturing images of hydraulic conveying flow with a small amount of solid sediment. ERT can also be used to capture the

solid distribution and online solid deposition in hydraulic slurry conveying systems. This has been further developed to enable real-time imaging of solid deposition in pipeline systems, and through use of multiple electrode planes disposed along the pipe, it is possible to cross-correlate signals between adjacent planes in order to elucidate information on velocity (Lucas et al., 1999; Williams, 2005). For example, the detailed flow structure of swirling suspensions in pipelines can be sensed and used to optimize operational conditions (Wang et al., 2003) and to develop strategies for unblocking plugged pipelines. Such methods are in use industrially (Primrose, 2008).

3.3.3 Visualization of dispersions in an oscillatory baffled reactor

Formulation of multi-component emulsions and mixtures are of interest in chemical and industrial processes (Vilar, 2008; Vilar et al., 2008). Standard stirred tank reactors (STR) and oscillatory baffled reactors (OBR) are traditional methods for the formulation of liquid–liquid mixtures and liquid–solid emulsions. Compared with STR, oscillatory baffled reactors provide more homogeneous conditions and uniform mixing with a relatively lower shear rate (Gaidhani et al., 2005; Harrison and Mackley, 1992; Ni et al., 2000). Figure 17 is a sketch of a typical oscillatory baffled reactor. It consists of the reactor vessel, orifice plate baffles, and an oscillatory movement part. The orifice plate baffles play an important role in the OBR for the vertex generation in the flow vessels as well as the radial velocities of the emulsions and mixtures. They are equally spaced in the vessel with a free area in the center of each baffle

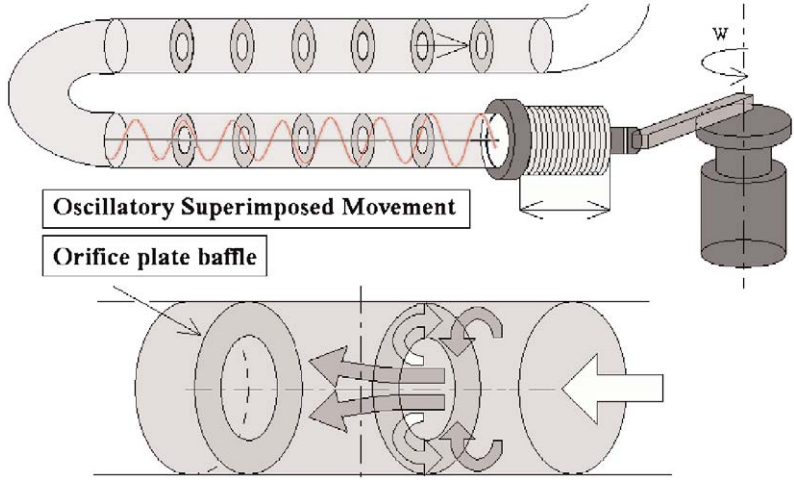

Figure 17 Sketch of the oscillatory baffled reactor (top) and flow within baffled sections (bottom).

for the fluid to flow. The part of oscillatory movement places an oscillatory motion on the fluid and, with the specific baffles, provides good axial/radial mixings for the working fluids and solids with highly efficient heat and mass transfer. A mineral oil, with a light density of 850 kg/m^{3}working as a dispersed phase, is introduced in droplet form into the continuous phase water flow with a high density of 997 kg/m^{3}at the top of the flow vessel. Figure 18 shows images of local oil fraction distributions in oscillatory baffled reactor obtained by ERT (Vilar et al., 2008). The green and blue colors represent low and high conductivity materials which are oil and water, respectively. The oil volume fraction could be calculated based on the conductivity map of the OBR. The oil phase is introduced at the top of the reactor and can be seen at the top of the images on the upper left section of Figure 18. The vortex formed from the oscillatory movement and the baffles enhance the mixing of oil and water. By using adjacent electrode rings (lower right, Figure 18), characteristics of the velocities of the phases can be seen (upper right and lower left). Here we see that ERT is used to visualize dispersions in the oscillatory baffled reactors and can give clear and quantitative mapping of the emulsions and mixtures of liquid–solid and liquid–liquid flows. Use of high-speed ERT systems operating at more than 1000

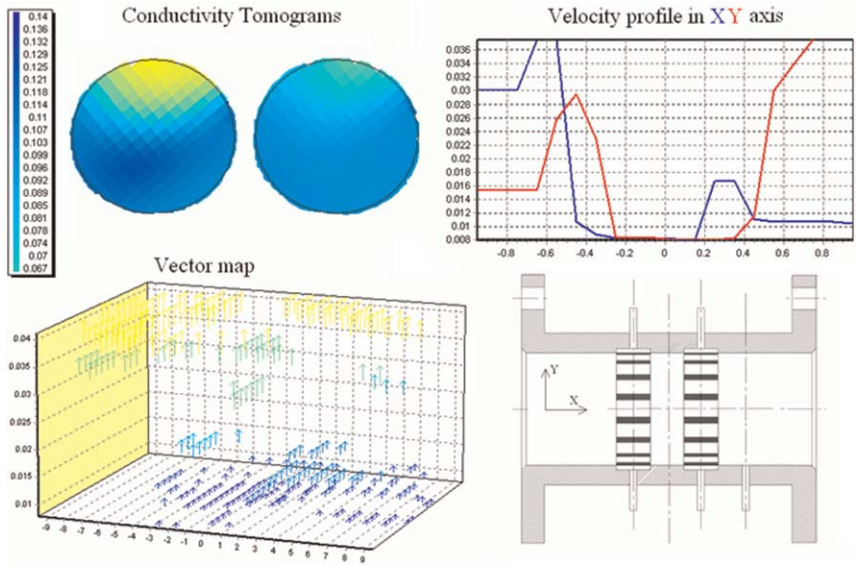

Figure 18 Tomographic images of local oil fraction distributions in oscillatory baffled reactor (top left), with estimated velocity profiles (top right) from cross-correlation signals between adjacent electrode rings (bottom right) and vector map (bottom left) (Vilar et al., 2008; Vilar, 2008) (see Plate 15 in Color Plate Section at the end of this book).

frames per second have enabled abstraction of concentration and velocity data in the reactor and synchronization of images with the stroke of the pulsed reactor to elucidate detailed information on inter-stage mixing (Issa et al., 2009).

4. POSITRON EMISSION TOMOGRAPHY

4.1 Introduction

Positron emission tomography is a radioisotope emission technique widely used in diagnostic medicine and has found new applications outside the medical field (Hoffmann, et al. 2005; Parker and McNeil, 1996). PET is a specific type of GRT techniques. For the PET technique, a radioactive source or tracers is introduced into the selected component of a multi-component system. The decay of two back-to-back γ-rays generated by radioactive tracers is monitored by external detectors. Back-projection techniques are used to obtain the distribution of the tracers in the monitoring region, from which the multi-component flow structure in the monitoring region is obtained. PET is a widely used technique for tracking multi-phase flows in engineering studies.

4.2 Principle of PET

In PET, radioactive tracers are introduced into a selected component of a multi-component system. Emission of a positron, which is the anti-particle of the electron having the same mass and equal but opposite charge, as one of its decay products is involved in the form of β-decay from the radioisotope. Two back-to-back 511 keV γ-rays are formed by the annihilation of the positron and the electron. External position-sensitive detectors are used to monitor the straight line formed by the two back-to-back γ-rays or the line along which the annihilation has taken place. The back-to-back γ-rays pair detected by the two separate external position sensitive detectors should be within a coincidence resolving time of approximately 20 ns. The number of γ-rays along each line is accurately and quantitatively measured by the two separate external position-sensitive detectors to reflect the tracer density integrated along the line, or called a ''projection.'' The entire tracer distribution in the monitoring region is provided by the back-projection techniques imposed on measurements of all possible projections (Benton and Parker, 1997). The flow structure of the selected component in the multi-component system is then obtained. Medical PET scanners or cameras have been extensively developed in the past 30 years. A typical medical PET scanner consists of a ring of scintillators to provide a 2D image of the tracer distribution in

the slice of the ring. More coaxial rings of scintillators provide extended 2D images or even fully 3D images of the tracer distribution. The most famous non-medical PET camera is the Brimingham positron camera (Hawkesworth et al., 1986; Parker and McNeil, 1996), which is shown in Figure 19. The camera consists of two external position-sensitive detectors, each having an area of $600 \times 300\,\text{mm}^2$. The camera takes a 2D picture of the plane parallel to the detector faces. Three-dimensional high-resolution images are obtained by rotating the detectors around the monitored object. Methods based on single particle tracking and multiple particle tracking are under development with the aim to design and use labels that are well matched to the measurement system under investigation. Work on the hardware is also seeking to develop versions of the equipment that are higher resolution and more portable for on-site use at suitable industrial plants.

The absorption and scattering of the γ-rays in the presence of matter between the tracers and the detectors, such as human bones and body tissues in medical application as well as vessel walls and internals of a multi-phase flow system in non-medical application, will introduce

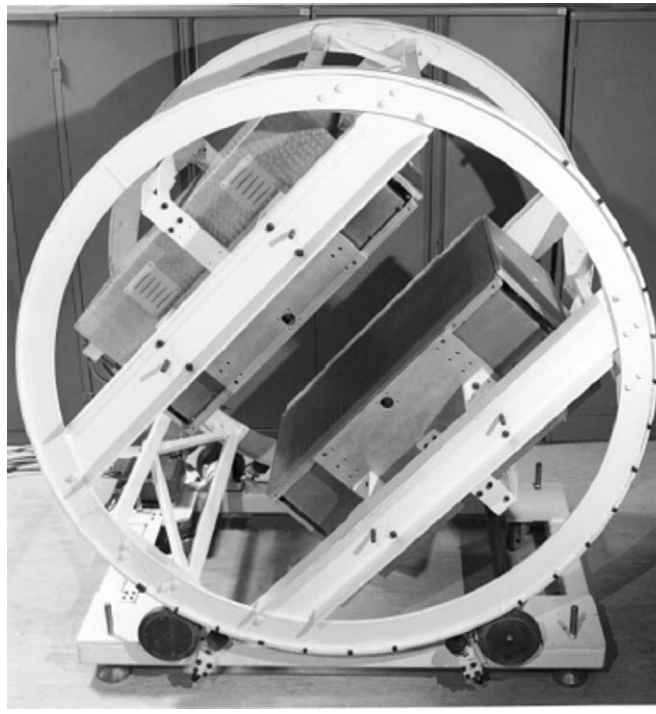

Figure 19 Photography of the first Birmingham University positron camera for industrial imaging (Parker and McNeil, 1996).

signal loss of the γ-rays. In medical applications, reduction of signal intensity is a key problem since the amount of radioactive tracers needs to be at a minimum in order to not threaten patient's health. However, in industrial applications, reduction of signal intensity is not a problem since the amount of radioactive tracers is of little concern; PET is thus a more easy to use technique for tracking multi-phase flows in engineering studies.

4.3 PET applications

4.3.1 Slurry mixtures in stirred tanks

Slurry mixing of opaque multi-phase flow systems is intensively developed in pharmaceuticals, polymers, and food industries. Fundamental understanding of the hydrodynamics of slurry mixing behavior in opaque multi-phase flow systems is of great importance for the design and optimization of the STR. The operating conditions for the STRs, such as the minimum stirrer-spinning speed of the impeller to suspend all the solids/liquid in the reactor without any dead zone and the stirrer speed to provide homogeneous solid–liquid/liquid–liquid emulsions and mixtures, need to be determined to obtain high-quality products (Barigou, 2004). PET has the capability to track the movements and concentrations of one component, such as sand particles or selected fluids, in a multi-component system. Figure 20 shows a PET image of the sand concentration distribution of the sand–water slurry in a STR with a cylindrical vessel shape (McKee et al., 1995b). Pure coarse sands with a diameter of 600–700 μm were used as the suspended solids in the left image, whereas a mixture consisting of 80% coarse sands and 20% fine sands with a diameter of 150–210 μm were used in the right image. The two figures show only the coarse sand concentration distribution since only the coarse sands were traced with radioactive tracers. The gray scale

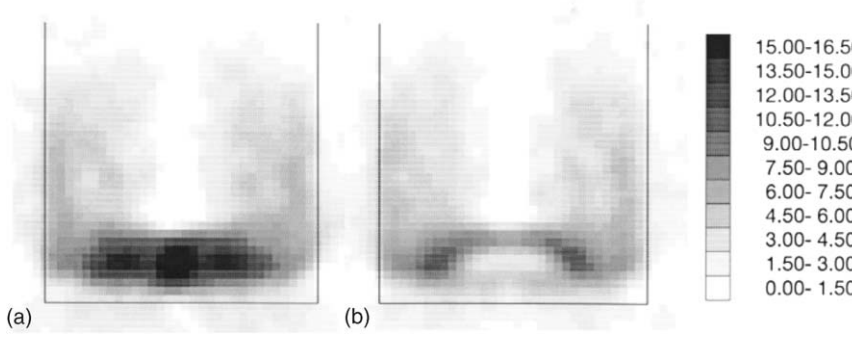

Figure 20 Tomographic sand distribution in slurry mixtures (McKee et al., 1995b).

shows the volume percentage of coarse sands in the reactor. Noise exists outside the reactor and has a value less than 3%. The single projected view of the STR provides a 3D solid distribution, since the axial stirrer in the cylindrical vessel provides a solids distribution with rotational symmetry (McKee et al., 1995b). Images of the sand concentration distribution in a sand–water STR demonstrate the capability of PET in tracking multi-phase flow in engineering applications. A number of studies have been performed on multi-phase systems in process equipment (Conway-Baker et al., 2002; West et al., 1999) and also detailed comparisons of the dynamic granular flow models in which predictions from discrete elements models are compared with real behaviors (e.g., Link et al., 2008).

4.3.2 Dispersion of particle pulse in gas—solid fluidized beds

Gas–solid fluidized bed technology provides high mass and heat-transfer coefficients between gas and solids in the reactor. It has been applied widely in industries such as the oil, metallurgical, and chemical industries (Fan and Zhu, 1998; Kunni and Levenspiel, 1991). Although gas–solid fluidization has been developed for several decades and considerable research results on hydrodynamics of the fluidized beds have been achieved, accurate solid movement and dispersion in gas-solid fluidized beds are still required for the industrial design, operation, and fundamental understanding of gas–solid fluidized beds. PET is an effective technique to accurately record the movement and dispersion of solids in these reactors. For dispersion of solid measurements in the fluidized beds, the tracer solids should have the same physical properties and fluidization characteristic as the bulk solids. Dechsiri et al. (2005b) studied the dispersion of particle pulse in a gas–solid fluidized bed. The FCC catalyst particles (Geldart group A) with an average of 79.5 μm and a density of 1464 kg/m^3 are used for the bulk and tracer solids in the bed. Three grams of FCC solids are labeled with radioactive material and uniformly placed at the surface of the bed as the tracers. The fluidized bed is made of a cylindrical glass column with a height of 35 cm and diameter of 15 cm. A cylindrical PET camera is located outside the fluidized bed vessel to capture the movement and dispersion of the tracer. Figure 21 depicts a PET image of the dispersion of pulses initially placed at the surface of a gas–solid fluidized bed (Dechsiri et al., 2005b). The numbers at the top of Figure 21 are the particle pulse positions and movements over the range of 12 s. The two numbers at the bottom of Figure 21 are the 3D and contour plots of relative averaged intensity of the tracer solid concentration in the horizontal plane of the fluidized bed vs. height in the bed and time, respectively. The dispersion of the solids shows asymmetry on the two sides of the axis of the fluidized bed. The images of the tracer solids movement and dispersion show that the

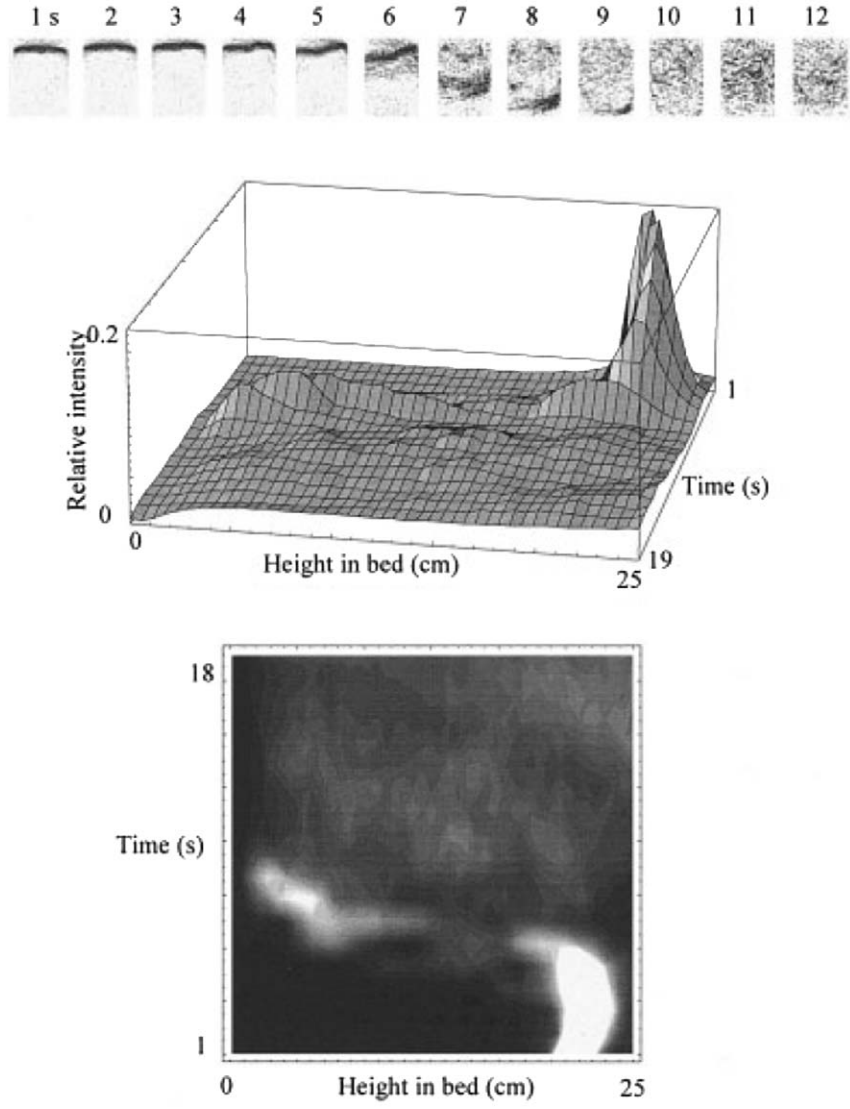

Figure 21 Dispersion of particle pulse initially placed at the surface of a gas–solid fluidized bed (Dechsiri et al., 2005b).

downward velocity of the pulse solids in the bulk phase has a value of 0.05 m/s.

4.3.3 Visualization of multi-phase fluids through sudden expansions

Sudden expansions of beds are very common in many industrial facilities such as heat exchange, mixing, and feeding systems (Arola et al., 1998).

Owing to limited measurement techniques, understanding the mechanism of the particle dispersion through sudden expansions is still a fundamental research topic. Particle collisions effect the particle concentration and introduce inhomogeneity in the suspensions. Accurate and quantitative measurements of the opaque flow behaviors through sudden expansions are needed. PET has been successfully applied for non-intrusive measurements of pipe flows of solids suspensions such as papermaking and pulp suspensions. The behavior of papermaking fiber suspension passing through a sudden expansion has been studied using PET (Heath et al., 2007). The papermaking fibers are labeled using Fluorine-18 (^{18}F). The concentration profiles are reflected by the radioactivity distribution obtained by a PET camera. Figures 22 and 23 contain PET images (a. top view; b. cross-section view; c. side view; d. 3D

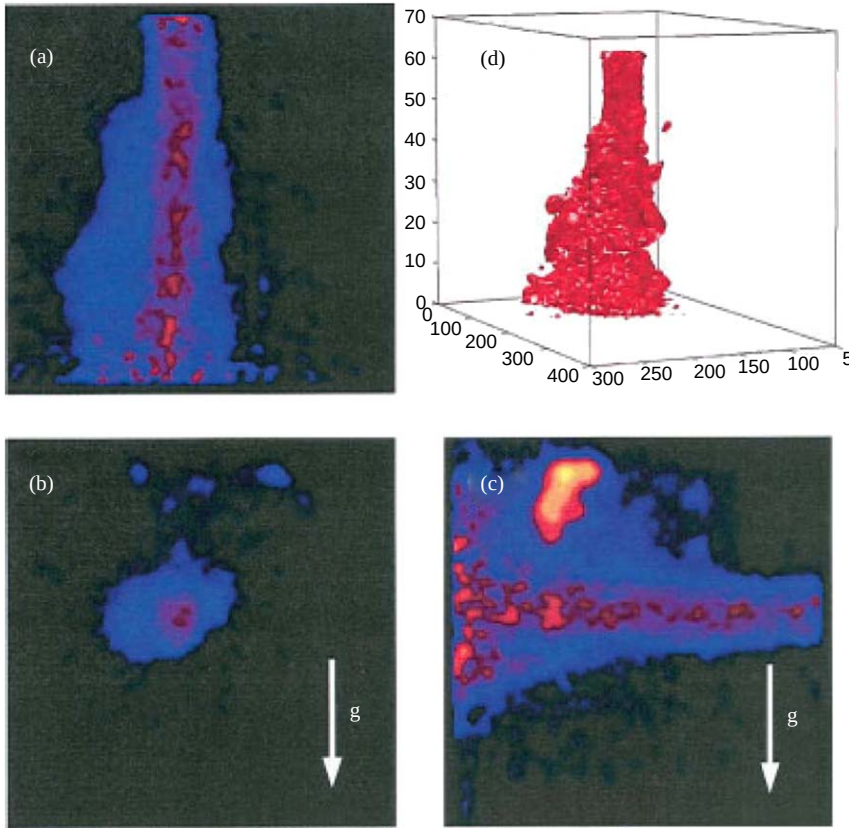

Figure 22 Flow of a fiber suspension through a sudden expansion with an upstream velocity of 0.5 m/s (Heath et al., 2007) (see Plate 16 in Color Plate Section at the end of this book).

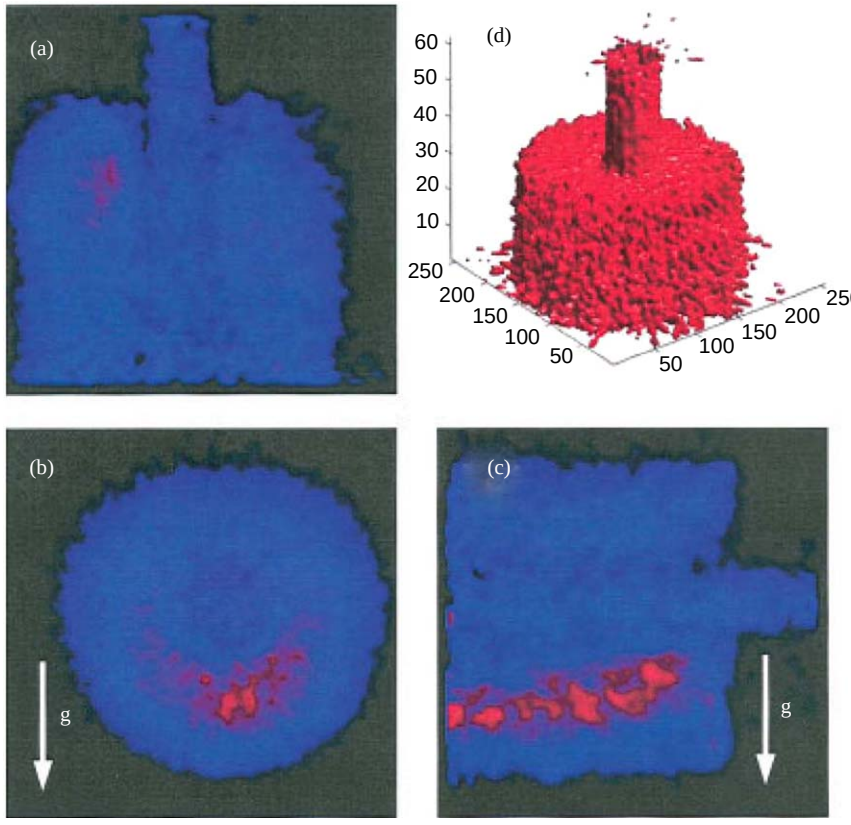

Figure 23 Flow of a fiber suspension through a sudden expansion with an upstream velocity of 0.7 m/s (Heath et al., 2007) (see Plate 17 in Color Plate Section at the end of this book).

reconstruction of the tracer distribution) of the concentration profiles of the papermaking fiber suspension through the sudden expansion with the upstream velocity of 0.5 m/s and 0.7 m/s, respectively (Heath et al., 2007). At a low upstream velocity of 0.5 m/s, the papermaking fibers are not well-mixed after passing through the expansion part due to low shear from the fluid, which is characterized as "plug flow." At a high upstream velocity of 0.7 m/s, the papermaking fibers are well-mixed after passing through the expansion part due to high shear from the fluid, which is defined as "fluidized" (Heath et al., 2007). PET measurements provide the quantitative 3D concentration of the papermaking fiber suspension passing through the sudden expansion. PET shows its solid capability for visualization of solids suspension multi-phase flow behaviors through sudden expansions.

5. CONCLUDING REMARKS

In this review, tomography systems of capacitance (ECT), resistance (ERT), and positron emission (PET) are presented. Their applications in imaging industrial processes highlight the importance and advantages of each technique. However, the common favored advantage among the three techniques is their ability to provide non-invasive measurements of various processes.

Principles of ECT and the latest developments in the technology are highlighted with emphasis on the volume ECT (ECVT) for 3D imaging. The significance of ECT technique in process engineering is presented in the framework of industrial application. Fluidized beds, pneumatic solids conveying, and slurry bubble columns are examples of ECT's capability to provide quantitative and qualitative understanding of the internal process dynamics.

ERT is presented of its similarities to ECT as both techniques are governed by similar equations of electrical field and current distributions. Examples of ERT in hydrocyclone flow visualization, comparison with CFD, high-speed flow imaging in slurry conveying, and visualization of dispersions in an oscillatory baffled reactor are discussed to highlight applicability of ERT in industrial processes. Both ECT and ERT are electrical modalities for process imaging and share the common characteristics of high imaging speed, safety, suitability for various sizes of vessels, and non-linearity of interrogating signals in regard to phase distribution.

PET, on the other hand, is a radioactive modality of tomography. Examples of PET applications in industrial process include imaging of slurry mixtures in STR, dispersion of particle pulse in gas–solid fluidized beds, and visualization of multi-phase fluids through sudden expansions. Although such methods require sophisticated facilities, due to the nature of the radiation source, they provide accurate data for detailed model comparison which is of major benefit for industrial design and operation.

NOMENCLATURE

NOTATION

C	$1 \times N$ measured vector of capacitances between the n_c electrode pairs
C_i	capacitance between the source and the detector electrodes for the i^{th} electrode
c	vector representing the boundary current

f_i	entropy objective function
f_{mse}	MSE function of G
f_s	smoothness function
G	$1 \times M$ image vector (permittivity distribution in the domain)
G^k	estimated permittivity vector in the kth iteration
$G_{s,tr}$	transport solids circulation rate
N	number of ERT electrodes
$\hat{n}$	normal vector to Γ_i
n_e	number of capacitor electrodes
Q_i	charge in the detector electrode for the ith electrode pair
S	$N \times M$ sensitivity matrix
S^T	transposed matrix of S
U_g	gas velocity
U_{tr}	transport velocity
ΔV_i	voltage difference for the ith electrode pair
X	$N \times N$ uniformity matrix
Y	global admittance matrix

GREEK LETTERS

α	relaxation factor
Γ_i	closed curve enclosing the detector electrode
$\gamma_1, \gamma_2, \gamma_3$	normalized constants between 0 and 1
$\varepsilon(x, y)$	dielectric constant (permittivity) distribution
$\phi(x,y)$	potential distribution
ν	vector representing the potentials of the mesh-node point

REFERENCES

Abdullah, M. Z., Electrical impedance tomography for imaging conducting mixtures in hydrocyclone separators. PhD Thesis, UMIST (1993).

Arola, D., Powell, R. L., McCarthy, M. J., Li, T. Q., and Odberg, L. *AIChE J.* **44**, 2597–2606 (1998).

Barber, D. C. *Clin. Phys. Physiol. Meas.* **11**, 45–46 (1990).

Barber, D. C., Brown, B. H., and Freeston, I. L. *Electron. Lett.* **19**, 933–935 (1983).

Barigou, M. *Chem. Eng. Res. Des.* **82**(A9), 1258–1267 (2004).

Baumgarten, P. K., and Pigford, R. L. *AIChE J.* **6**, 115–123 (1960).

Bayle, J., Mege, P., and Gauthier, T., Dispersion of bubble flow properties in a turbulent FCC fluidized bed, *in* "Proceedings of 10th Engineering Foundation Conference, *Fluidization X*" (M. Kwauk, J. Li, and W.-C. Yang Eds.), pp. 125–132. Beijing, China (2001).

Bennett, M. A., and Williams, R. A. *Min. Engn.* **17**, 605–614 (2004).

Bennett, M. A., West, R. M., Luke, S. P., Jia, X., and Williams, R. A. *Chem. Eng. Sci.* **54**(21), 5003–5012 (1999).

Benton, D. M., and Parker, D. J., Non-medical applications of positron emission tomography, *in* ''Non-Invasive Monitoring of Multiphase Flows'' (J. Chaouki, F. Larachi, and M. P. Dudukovic Eds.), pp. 161–184. Elsevier Science, New York (1997).

Binns, R., Lyons, A. R. A., Peyton, A. J., and Pritchard, W. D. N. *Meas. Sci. Technol.* **12**, 1132–1138 (2001).

Boyer, C., and Fanget, B. *Chem. Eng. Sci.* **57**, 1079–1089 (2002).

Breckon, W. R., and Pidcock, M. K. Mathematical aspects of impedance imaging, *Clin. Phys. Physiol. Meas. A* **8**, 77–84 (1987).

Chen, R. C., Reese, J., and Fan, L.-S. *AIChE J.* **40**, 1093–1104 (1994).

Chocha, F., Castro, B., Ovalle, E., and Romero, J. *Phys. Separ. Technol.* 35–60 (1998).

Clough, D. E., and Weimer, A. W. *Ind. & Eng. Chem. Fund.* **24**(2), 235–241 (1985).

Conway-Baker, J., Barley, R. W., Williams, R. A., Jia, X., Kostuch, J., McLoughlin, B., and Parker, D. J. *Min. Engn.* **15**(1-2), 53–59 (2002).

Cui, H., and Chaouki, J. *Chem. Eng. Sci.* **59**(16), 3413–3422 (2004).

Cullivan, J. C., and Williams, R. A. *Part. Sci. Technol*, **21**, 83–103 (2003).

Cullivan, J. C., and Williams, R. A., Velocity, size and shape and concentration measurements of particulate mixtures. Chapter 14.4, *in* ''*Multiphase Flow Handbook*'' (C. Crowe Ed.), pp. 42–87. Taylor and Francis, London CRC Mechanical Engineering Series (2005).

Cullivan, J. C., Williams, R. A., Dyakowski, T., and Cross, C. R. *Min. Engn.* **17**, 651–660 (2004).

Dechsiri, C., Ghione, A., van de Wiel, F., Dehling, H. G., Paans, A. M. J., and Hoffmann, A. C. *Can. J. Chem. Eng.* **83**(1), 88–96 (2005a).

Dechsiri, C., van der Zwan, E. A., Dehling, H. G., and Hoffmann, A. C. *AIChE J.* **51**(3), 791–801 (2005b).

Dickin, F., and Wang, M. *Meas. Sci. Technol.* **7**, 247–260 (1996).

Du, B., and Fan, L.-S. *Ind. & Eng. Chem. Res.* **43**(18), 5507–5520 (2004b).

Du, B., Warsito, W., and Fan, L.-S. *AIChE J.* **49**(5), 1109–1126 (2003).

Du, B., Warsito, W., and Fan, L.-S. *AIChE J.* **50**(7), 1386–1406 (2004a).

Du, B., Warsito, W., and Fan, L.-S. *Ind. & Eng. Chem. Res.* **44**(14), 5020–5030 (2005).

Dyakowski, T., and Williams, R. A., Hydrocyclone flow modeling—a continuous research challenge, Chapter 5, *in* ''*Innovation in Physical Separation Technologies: Richard Mozley Symposium Volume*,'' The Institution. Mining & Metallurgy, London, pp. 61–73 (1998).

Fan, L.-S., and Zhu, C., ''Principles of Gas-Solid Flows''. Cambridge University Press, New York (1998).

Fan, L. T., Ho, T. C., Hiraoka, S., and Walawender, W. P. *AIChE J.* **27**, 388 (1981).

Fangary, Y. S., Williams, R. A., Neil, W. A., Bond, J., and Faulks, I. *Powder Technol.* **95**, 61–66 (1998).

Fennell, P. S., Davidson, J. F., Dennis, J. S., Gladden, L. F., Hayhurst, A. N., Mantle, M. D., Mueller, C. R., Rees, A. C., Scott, S. A., and Sederman, A. J. *Chem. Eng. Sci.* **60**(7), 2085–2088 (2005).

Gaidhani, H. K., McNeil, B., and Ni., X. *Trans IChemE, Part A, Chem. Eng. Res. Des.* **83**(A6), 640–645 (2005).

Geldart, D., and Kelsey, J. R. *Powder Technol.* **6**(1), 45–50 (1972).

Geldart, D., and Xie, H. Y. *Fluid. VII, Proc. Eng. Found. Conf. Fluid.* 749–756 (1992).

George, A., and Liu, J. W., ''Computer solution of large positive definite sparse matrices''. Prentice-Hall, New York (1995).

George, D. L., Torczynski, J. R., Shollenbeger, K. A., O'hen, T. J., and Ceceio, S. L. *Int. J. Multiphase Flow* **26**, 549–581 (2000).

Gibilaro, L. G., Di Felice, R., Foscolo, P. U., and Waldram, S. P. *Chem. Eng. J.* **37**, 25–33 (1988).

Gilbertson, M. A., Cheesman, D. J., and Yates, J. G., Observations and measurements of isolated bubbles in a pressurized gas-fluidized bed. Fluidization IX, Proceedings of the Engineering Foundation Conference on Fluidization 9th, Durango, CO, United States, May 17–22, 61–68 (1998).
Gunn, D. J., and Al-Doori, H. H. *Int. J. Multiphase Flow,* **11**, 535–551 (1985).
Halow, J. S., and Nicoletti, P. *Powder Technol.* **69**(3), 255–277 (1992).
Harrison, S. T. L., and Mackley, M. R. *Chem. Eng. Sci.* **47**(2), 490–493 (1992).
Hawkesworth, M. R., O'Dwyer, M. A., Walker, J., Fowles, P., Heritage, J., Stewart, P. A. E., Witcomb, R. C., Bateman, J. E., Connolly, J. F., and Stephenson, R. *Nucl. Instrum. Methods A* **253**, 145–157 (1986).
Heath, S. J., Olson, J. A., Buckley, K. R., Lapi, S., Ruth, T. J., and Martines, D. M. *AIChE J.* **53**, 327–334 (2007).
Ho, T. C., Yutani, N., Fan, L. T., Walawender, W. P., and Song, J. C. *Chem. Eng. Sci.* **38**(4), 575–582 (1983).
Hoffmann, A. C., Dechsiri, C., Van der Zwan, E. A., and Dehling, H. G. *AIChE J.* **51**(3), 791–801 (2005).
Holland, D. J., Marashdeh, Q., Muller, C. R., Wang, F., Dennis, J. S., Fan, L.-S., and Glandden, L. F. *Ind. Eng. Chem. Res.* **48**, 172–181 (2009).
Hua, P., Webster, J. G., Tompkins, W. J., Effect of the measurement method on noise handling and image quality of EIT imaging, IEEE 9th Annual Conference on Engineering in Medicine and Biological Science, pp. 1429–1430 (1993).
Huang, S. M., Plaskowski, A., Xie, C. G., and Beck, M. S. *J. Physica E* **22**, 173–177 (1989).
Hubers, J. L., Striegel, A. C., Heindel, T. J., Gray, J. N., and Jensen, T. C. *Chem. Eng. Sci.* **60**(22), 6124–6133 (2005).
Hulme, I., and Kantzas, A. *Powder Technol.* **147**(1-3), 20–33 (2004).
Issa, M., Wang, M., Vilar, G. and Williams, R. A., Measurements using high speed EIT on an oscillatory flow reactor 3rd International Tomography Workshop Japan, Tokyo, May (2009).
Jin, H., Wang, M., and Williams, R. A. *Chem. Eng. J.* **130**(2-3), 179–185 (2006).
Kai, T., Misawa, M., Takahashi, T., Tiseanu, I., and Ichikawa, N. *Can. J. Chem. Eng.* **83**(1), 113–118 (2005).
Kaipio, J., Duncan, S., Seppänen, A., Somersalo, E., and Voutilainen, A., *in* "Process imaging for automatic control" (D. Scott, and H. McCann Eds.), Taylor & Francis Group, Boca Raton (2005).
Kang, W. K., Sutherland, J. P., and Osberg, G. L. *Ind. & Eng. Chem. Fund.* **6**(4), 499–504 (1967).
Kantzas, A., and Kalogerakis, N. *Chem. Eng. Sci.* **51**(13), 3555 (1996).
Kim, B., Isaacson, D., Xia, H., Kao, T., Newell, J. C., and Saulnier, G. J. *Physiol. Meas.* **28**, 237–246 (2007).
Kotre, C. J. *Clin. Phys. Physiol. Meas.* **11**, 275–281 (1989).
Kotre, C. J. *Phys. Meas. A* **15**, 125–136 (1994).
Kunni, D., and Levenspiel, O., "Fluidization Engineering". Butterworht-Heinemann, Stoneham (1991).
Lanneau, K. P. *Transactions of the Institution of Chemical Engineers* **38**(3), 125–143 (1960).
Larachi, F., and Chaouki, J. *Recents Progres en Genie des Procedes* **14**(75), 347–353 (2000).
Larachi, F., Chaouki, J., Kennedy, G., and Dudukovic, M. P. Non-Invasive Monitoring of Multiphase Flows. 335–406. Elsevier Science, New York (1997).
Laskovski, D., Stevnson, P., Zhou, J., and Galvin, K. P. *Powder Technol.* **179**, 59–64 (2007).
Lim, E. W. C. *Chem. Eng. Sci.* **62**, 4529–4543 (2007).
Link, J. M., Deen, N. G., Kuipers, J. A. M., Fan, X., Ingam, A., Parker, D. J., Wood, J., and Seville, J. P. K. *AIChE J.* **54**(5), 1189–1202 (2008).
Lirag, R. C., and Littman, H. *Chem. Eng. Prog. Symp. Series* **67**(116), 11–22 (1971).

Liu, J., Grace, J. R., and Bi, X. *AIChE J.* **49**(6), 1405–1420 (2003a).
Liu, J., Grace, J. R., and Bi, X. *AIChE J.* **49**(6), 1421–1432 (2003b).
Loh, W. W., Array processor for use in electrical impedance tomography. MSc Thesis UMIST (1994).
Lucas, G. P., Cory, J., Waterfall, R., Loh, W. W., and Dickin, F. J. *J. Flow Meas. Instrum.* **10**, 249–258 (1999).
Marashdeh, Q., Fan, L.-S., Du, B., and Warsito, W. *Ind. Eng. Chem. Res.* **47**, 3708–3719 (2008).
McKee, S. L., Dyakowski, T., Williams, R. A., Bell, T. A., and Allen, T. *Powder Technol.* **82**(1), 105–114 (1995a).
McKee, S. L., Parker, D. J., and Williams, R. A., Visualization of size-dependent particle segregation in slurry mixers using positron emission tomography, *in* "Frontiers in Industrial Process Tomography" (D. M. Scott, and R. A. Williams Eds.), pp. 249–259. AIChE and Engineering Foundation, New York (1995).
Nakajima, M., Harada, M., Asai, M., Yamazaki, R., and Jimbo, G., Bubble fraction and voidage in an emulsion phase in the transition to a turbulent fluidized bed, *in* "Circulating Fluidized Bed III" (P. Basu, M. Horio, and M. Hasatani Eds.), p. 79. Pergamon, Oxford (1991).
Ni, X., Cosgrove, J. A., Arnott, A. D., Greated, C. A., and Cumming, R. H. *Chem. Eng. Sci.* **55**, 3195–3208 (2000).
Okhi, K. and Shirai, T., Particle velocity in a fluidized bed, in "*Fluidization Technology*" (D. L. Keairns Ed.), Hemisphere, New York (1976).
Orcutt, J. C., and Carpenter, B. H. *Chem. Eng. Sci.* **26**(7), 1049–1064 (1971).
Ormiston, R. M., Mitchell, F. R. G., and Davidson, J. F. *Trans. Inst. Chem. Eng.* **43**(7), T209–T216 (1965).
Ostrowski, K. L., Dyakowski, T., Luke, S. P., and Williams, R. A. *Powder Technol.* **104**, 287–295 (1999).
Ostrowski, K. L., Luke, S. P., Bennett, M. A., and Williams, R. A. *Chem. Eng. J.* **77**(1-2), 43–50 (2000).
Parker, D. J., and McNeil, P. A. *Meas. Sci. Technol.* **7**, 287–296 (1996).
Patel, A. K., Waje, S. S., Thorat, B. N., and Mujumdar, A. S. *Powder Technol.* **185**, 239–250 (2008).
Peters, M. H., Fan, L.-S., and Sweeney, T. L. *Chem. Eng. Sci.* **38**(3), 481–485 (1983).
Primrose, K, Industrial applications of electricial tomography: case studies, see www.itoms.com (Manchester) (2008).
Ross, A. S., An adaptive current tomograph for breast cancer detection, PhD Thesis, Rensselaer Polytechnic Institute, Troy, NY, USA (2003).
Rowe, P. N., and Masson, H. *Trans. Inst. Chem. Eng.* **59**(3), 177–185 (1981).
Rowe, P. N., and Matsuno, R. *Chem. Eng. Sci.* **26**(6), 923–935 (1971).
Rowe, P. N., and Partridge, B. A., X-ray study of bubbles in fluidized beds. *Trans. Inst. Chem. Engr.* (London) **43**(5), T157-T175 *Pub. in Chem. Engr. (London)* No. 189 (1965).
Rowe, P. N., and Yacono, C. X. R. *Chem. Eng. Sci.* **31**(12), 1179–1192 (1976).
Saulnier, G. J., Ross, A. S., and Liu, N. *Physiol. Meas.* **27**, 221–236 (2006).
Savelsberg, R., Demco, D. E., Blumich, B., and Stapf, S. *Phys. Rev. E: Statistical, Nonlinear, and Soft Matter Physics* **65**, 020301(R) (2002).
Schubert, M., Hessel, G., Zippe, C., Lange, R., and Hampe, U. *Chem. Eng. J.* **140**, 332–340 (2008).
Sharma, A. K., Tuzla, K., Matsen, J., and Chen, J. C. *Powder Technol.* **111**(1-2), 114–122 (2000).
Shi, T. M., C.G. Xie, C. G., Huang, S. M., Williams, R. A., and Beck, M. S. *Meas. Sci. Technol.* **2**, 923–933 (1991).
Sitnai, O. *Chem. Eng. Sci.* **37**(7), 1059–1066 (1982).

Smith, M., Bayle, J., and Gauthier, T., Bubble flow study in a turbulent FCC fluidized bed. *EFCE, European Congress of Chemical Engineering*, 2nd. Montpellier, October 5–7 47 (1999).

Somersalo, E., Cheney, M., and Isaacson, D. *SIAM J. Appl. Math.* **52**, 1023–1040 (1992).

Vilar, G., On-line measurement of dispersions in an oscillatory baffled reactor using electrical impedance tomography, PhD Thesis, University of Leeds, Leeds UK (2008).

Vilar, G., Williams, R. A., Wang, M., and Tweedie, R. J. *Chem. Eng. J.* **141**, 58–66 (2008).

Wang, M., Electrical impedance tomography on conducting walled vessels, PhD Thesis, UMIST, Manchester UK (1994).

Wang, M. *Meas. Sci. Technol.* **13**, 101–117 (2002).

Wang, M., Dickin, F. J., and Williams, R. A., Electrical resistance tomography, UK and world-wide patent application 9404766.9 (11 March 1994).

Wang, S. J., Dyakowski, T., Xie, C. G., Williams, R. A., and Beck, M. S. *Chem. Eng. J. (Lausanne)* **56**(3), 95–100 (1995).

Wang, Z. C., Afacan, A., Nandakumar, K., and Chuang, K. T. *Chem. Eng. Process.* **40**, 209–219 (2001).

Wang, M., Jones, T. F., and Williams, R. A. *Trans. IChemE* **81**(Part A8), 854–861 (2003).

Wang, M., Ma, Y., Holliday, N., Dai, Y., Williams, R. A., and Lucas, G. *IEEE Sensors Journal* **5**(2), 289–299 (2005).

Wang, F., Marashdeh, Q., Warsito, W., and Fan, L.-S., Imaging gas/solid jet penetration in a gas-solid fluidized bed using electrical capacitance volume tomography, AIChE Annual Meeting, Philadelphia, PA, USA, 16–21 November, Section 03B01 (2008).

Warsito, W., and Fan, L.-S. *Chem. Eng. Sci.* **56**, 6455–6462 (2001a).

Warsito, W., and Fan, L.-S. *Meas. Sci. Technol.* **12**, 2198–2210 (2001b).

Warsito, W., and Fan, L.-S. *Chem. Eng. Sci.* **58**, 823–832 (2003).

Warsito, W., and Fan, L.-S. *Chem. Eng. Sci.* **60**, 6073–6084 (2005).

Warsito, W., Marashdeh, Q., and Fan, L.-S. *IEEE Sens. J.* **7**, 525–535 (2007).

Weimer, A. W., Gyure, D. C., and Clough, D. E. *Powder Technol.* **44**(2), 179–194 (1985).

Werther, J. *Powder Technol.* **102**(1), 15–36 (1999).

Werther, J., and Molerus, O. *Int. J. Multiphase Flow* **1**, 103–122 (1973).

West, R. M., Jia, X., and Williams, R. A. *Chem. Eng. Commun.* **175**, 71–79 (1999).

West, R. M., Jia, X., and Williams, R. A. *Chem. Eng. J.* **77**(1-2), 31–36 (2000).

West, R. M., Scott, D. M., Sunshine, G., Kostuch, J. A., Heikkinen, L., Vauhkonen, M., Hoyle, B. S., Schlaberg, H. I., Hou, R., and Williams, R. A. *Meas. Sci. Technol.* **13**, 1890–1897 (2002).

West, R. M., Aykroyd, R. G., Meng, S., and Williams, R. A. *Physiol. Meas.* **25**, 181–194 (2004).

Wexler, A., Fry, B., and Neuman, M. R. *Appl. Opt.* **24**, 3985–3992 (1985).

Williams, R. A., Mineral and material processing, Chapter 11, *in* "Process Imaging for Automatic Control" (D. M. Scott, and H. McCann Eds.), pp. 359–400. Taylor and Francis (2005).

Williams, R. A., and Beck, M. S. (Eds.), Process tomography-principles, *in* "Techniques and Applications" p. 550. Butterworth-Heinemann, Oxford (1995).

Williams, R. A., Mann, R., Dickin, F. J., Ilyas, O. M., Ying, P., Edwards, R. B., and Rushton, A. *AIChE. Symp. Ser.* **293**, 8–15 (1993).

Williams, R. A., Jia, X., West, R. M., Wang, M., Cullivan, J. C., Bond, J., Faulks, I., Dyakowski, T., Wang, S. J., Climpson, N., Kostuch, J. A., and Payton, D. *Min. Engn.* **12**(10), 1245–1252 (1999).

Wu, C. N., Cheng, Y., Ding, Y. L., Wei, F., and Jin, Y. *Chem. Eng. Sci.* **62**, 4325–4335 (2007).

Xie, C. G., Image reconstruction, *in* "Process Tomography—Principles, Techniques and Applications" (R. A. Williams, and M. S. Beck Eds.), pp. 281–323. Butterworth-Heinemann, Oxford (1995).

Xie, C. G., Huang, S. M., Hoyle, B. S., Thorn, R., Lean, C., Snowden, D., and Beck, M. S. *IEE Proceedings G* **139**, 89–98 (1992).
Yang, W. Q., and Peng, L. *Meas. Sci. Technol.* **14**(1), R1–R13 (2003).
Yang, W. Q., Spink, D. M., York, T. A., and McCann, H. *Meas. Sci. Technol.* **10**, 1065–1069 (1999).
Yasui, G., and Johanson, L. N. *Am. Inst. Chem. Engrs. J.* **4**, 445–452 (1958).
Yates, J. G., and Simons, S. J. R. *Int. J. Multiphase Flow* **20**(Suppl., Annual Reviews in Multiphase Flow 1994), 297–330 (1994).
Yates, J. G., Cheesman, D. J., and Sergeev, Y. A. *Chem. Eng. Sci.* **49**(12), 1885–1895 (1994).
Yin, W. L., and Wang, H. X., Quantification of swirling flow in hydraulic conveying from resistance tomography images, *Instrumentation and Measurement Technology Conference* (Conference Proceedings, Vail, CO, USA), 20–22 May (2003).
Yorkey, T. J., Comparing reconstruction algorithms for electrical impedance tomography,'' PhD Thesis, University of Wisconsin (1986).
Yorkey, T. J., Webster, J. G., and Tompkins, W. J. *IEEE Trans. Biomed. Eng.* **34**, 843–852 (1987a).
Yorkey, T. J., Webster, J. G., and Tompkins, W. J. *IEEE Trans. Biomed. Eng.* **34**, 898–901 (1987b).